

A NUMERICAL STUDY OF CHARACTERISTIC SLOW-TRANSIENT BEHAVIOR OF A COMPRESSIBLE 2D GAS-LIQUID TWO-FLUID MODEL

H.A. FRIIS^{A,B}, S. EVJE^{A,*} AND T. FLÅTTEN^C

ABSTRACT. The purpose of this paper is to gain some insight into the characteristic behavior of a general compressible two-fluid gas-liquid model in 2D by using numerical computations. Main focus is on mass transport phenomena. Relatively few numerical results in higher dimensions can be found in the literature for this two-fluid model, in particular, for cases where mass transport dynamics are essential. We focus on natural extensions to 2D of known 1D benchmark test cases, like water faucet and gas-liquid separation, previously employed by many researchers for the purpose of testing various numerical schemes. For the numerical investigations, the WIMF discretization method introduced in [SIAM J. Sci. Comput. 26 (2005), 1449] is applied, in combination with a standard dimensional splitting approach. Highly complicated flow patterns are observed reflecting the balance between acceleration forces, gravity, interfacial forces, and pressure gradients. An essential ingredient in these results is the appearance of single-phase regions in combination with mixture regions (dispersed flow). Solutions are calculated and shown from early times until a steady state is reached. Grid refinement studies are included to demonstrate that the obtained solutions are not grid-sensitive.

Subject classification. 76T10, 76N10, 65M12, 35L65

Key words. two-fluid model, hyperbolic, numerical scheme, pressure-velocity coupling, single-phase flow

1. INTRODUCTION

The starting point for this paper is a general, isothermal compressible two-fluid model (2D variant) in the following form where the index l, g refers to a liquid and gas phase, respectively:

$$\begin{aligned} \frac{\partial(\alpha_g \rho_g)}{\partial t} + \nabla \cdot (\alpha_g \rho_g \mathbf{v}_g) &= 0, \\ \frac{\partial(\alpha_l \rho_l)}{\partial t} + \nabla \cdot (\alpha_l \rho_l \mathbf{v}_l) &= 0, \\ \frac{\partial(\alpha_g \rho_g \mathbf{v}_g)}{\partial t} + \nabla \cdot (\alpha_g \rho_g \mathbf{v}_g \otimes \mathbf{v}_g) + \alpha_g \nabla p + \Delta p \nabla \alpha_g &= \mathbf{Q}_g + \mathbf{M}_g, \\ \frac{\partial(\alpha_l \rho_l \mathbf{v}_l)}{\partial t} + \nabla \cdot (\alpha_l \rho_l \mathbf{v}_l \otimes \mathbf{v}_l) + \alpha_l \nabla p + \Delta p \nabla \alpha_l &= \mathbf{Q}_l + \mathbf{M}_l. \end{aligned} \tag{1}$$

Here α_g, α_l are the volume fractions which satisfy the relation $\alpha_l + \alpha_g = 1$. Furthermore, $\rho_l(p), \rho_g(p)$ are fluid densities, p is pressure, $\mathbf{v}_l, \mathbf{v}_g$ are fluid velocities, $\mathbf{Q}_l, \mathbf{Q}_g$ represent external forces (friction and gravity), $\mathbf{M}_l, \mathbf{M}_g$ represent interfacial forces modelling interactions between the two phases. In particular, $\mathbf{M}_l + \mathbf{M}_g = 0$.

The model must be supplemented with equations of state for the gas and liquid phase. Moreover, expressions must be given for the interphase drag force, typically in the form $\mathbf{M}_l = -\mathbf{M}_g = C(\alpha_g, \rho_l, \rho_g) |\mathbf{v}_g - \mathbf{v}_l| (\mathbf{v}_g - \mathbf{v}_l)$, see for example [11]. Similarly, expressions for $\mathbf{Q}_g, \mathbf{Q}_l$ must be specified. The Δp term is required in order to make the model well-defined. Several expressions

Date: January 16, 2009.

^AInternational Research Institute of Stavanger (IRIS), Prof. Olav Hanssensvei 15, NO-4068 Stavanger, Norway.

^BDepartment of informatics, University of Bergen, P.O.Box 7800, N-5020 Bergen, Norway.

^CSINTEF Energy Research, Sem Sælands vei 11, NO-7465 Trondheim, Norway.

*Corresponding author.

Email address: steinar.evje@iris.no.

for Δp have been proposed in the literature. In this work the purpose of the interface correction term Δp is to ensure that the model becomes hyperbolic (real eigenvalues), and may have little physical justification. We refer to [13] and references therein for more details.

Different discretization approaches. As described in the recent book edited by Prosperetti and Tryggvason [31] there are, roughly speaking, two different classes of discretization techniques that have been used for solving the two-fluid model. The first one is referred to as *segregated* methods, the second type as *coupled* methods. The distinction between these two is not very clear, nevertheless, by relating the various schemes to these two different groups it may be easier to identify similarities and differences.

Group I (segregated methods). Some characteristics of the first group are, see Chapter 10 in [31] for more details:

- A pressure evolution equation is solved in combination with the momentum equations in a sequential and iterative fashion, see for example Chapter 10.3 in [31];
- Use of a staggered grid where pressure, densities and volume fraction are associated with nodes whereas velocities are assigned the midpoints lying between the nodes. However, as described in Chapter 10 in [31], there are also "co-located" versions of these algorithms where all the dependent variables are defined at the center of a control volume;
- The algorithms are suitable for (relatively) slow transients;
- It is easy to add new equations due to the one-by-one solution strategy;
- Examples of such codes are MFIX and CFX;
- Typically, various semi-implicit time discretization techniques are used leading to iterative solution procedures (e.g. Newton or Picard linearization). As pointed out in Chapter 10.6 the convergence properties of these algorithms often demand small time steps in order to achieve a converged solution;
- Some of the algorithms seem to work for a relatively weak stability condition (time step restriction associated with the fluid flow velocity) by using a more coupled solution strategy instead of a pure sequential. The code Olga mentioned below is an example of this;
- Finite volume type discretization on unstructured grids has been used to obtain codes for solving problems in higher dimensions.

A partially coupled algorithm which still is natural to group among the segregated methods is represented by the commercial code Olga [3]. A key feature of this algorithm is that, by relying on relatively small time steps and on what amounts to a suitable correction term added to the pressure equation, it is possible to avoid the iteration procedures typical for the segregated methods. Similarly, work by Kunz et al. [26] is an example of a tendency toward more strongly coupled solution methods springing from the segregated approach.

Group II (coupled methods). Some of the characteristics of the second group of methods, at least some of the more recent developments, are (see also Chapter 11 in [31]):

- Use of non-staggered grid;
- Typical applications of these methods are to solve for fast transients;
- More or less information about the eigenstructure of the Jacobian associated with the first order system (first order spatial derivatives) is often required;
- Use of explicit time discretization, i.e., no or little use of iterations;
- Examples include Roe and Godunov based schemes;
- Extension to high-resolution schemes is obtained by using flux-limiter or slope-limiter techniques [27];
- These schemes are often associated with a strong stability condition (i.e. the time step must be related to the sonic speed);
- A dimensional splitting approach is often used for solving higher dimensional problems, but there are also examples of use of a finite volume approach.

For a few examples of works in this direction we refer to [37, 9, 10, 13, 30, 29]. In addition, various semi-implicit methods, based essentially on ideas of Liles and Reed [28], that naturally also fall

in this group of methods are those described in Chapter 11.2 in [31]. Examples of such codes are RELAP, TRAC, SIMMER. These methods are typically first order (in space) and involve a combination of implicit and explicit time discretization. The purpose of the implicit component is to remove strong stability conditions (time step restrictions), whereas explicit time discretization is used for reduced computational cost and better accuracy of certain waves.

Mixture Flux (MF) methods. More recently, by combining ideas from the above two groups of methods, explicit as well as hybrid explicit-implicit schemes were derived for solving the 4-equation isothermal two-fluid model in 1D [14, 15, 16]. Some characteristics of these schemes are:

- Splitting of the physical flux into two parts, a convective flux and a pressure flux. This gives a framework for separating out the slow and the fast waves and developing appropriate numerical fluxes. In particular, numerical fluxes are constructed that allow for an accurate resolution (at least similar to a first order Roe scheme) of the slow mass waves whose time step is not determined by the fast sonic waves;
- Use of non-staggered grid;
- Use of a pressure evolution equation which is coupled to the momentum equations, however solved in a non-iterative and conservative manner;
- Numerical fluxes for the convective terms of the mass equations are obtained as a combination of an upwind-based and centred-based discretization. The upwind direction is taken relative to the fluid velocity. The motivation for this approach is to combine accuracy and stability properties in a desired manner.
- In principle, new equations can naturally be added to the 4-equation model, although this aspect has to a minor extent been explored so far;
- The basic MF (mixture flux) discretization can be used to derive a numerical scheme for a general system of conservation laws [17]. In particular, the resulting scheme contains the FORCE scheme [5, 7, 35] as a special case when an explicit time discretization is employed.

A good feature of the proposed approach is that no iterations are used. This may be a potential advantage over the group of segregated methods, where the number of iterations required to reach a certain accuracy, typically increases as the discretization grid is refined [31]. Concerning the time discretization, both an explicit, weakly implicit (WIMF) and strongly implicit (SIMF) version were developed. The main difference between these three variants is the stability condition. The time step of the explicit version [15] must obey a CFL condition which involves the sonic speed, the time step of the weakly implicit [14] must obey a CFL condition which involves the fluid velocity, whereas the strongly implicit version [16] can give stable solutions for all time steps. For instance, this is the situation for a simple flow case like transport of a volume fraction disturbance with constant velocity and constant pressure. The same feature carries over to the water faucet problem mentioned below, see Section 4.2. For more general flow cases, the situation becomes more complicated since instabilities may develop due to, for example, effects from strong source terms (stiffness of the source terms) and/or special problems related to transition to single-phase flow.

Various simulation results. Many schemes have been developed and tested in a 1D-setting [37, 9, 10, 13, 30, 29]. Classical test cases are various Riemann problems, water faucet [32], and gas-liquid separation [9]. This is convenient since approximate analytical solutions can be calculated and used to validate the quality of the numerical solutions. The two last examples represent mass transport dynamics taking place on a time scale of the order of seconds, and involve sharp volume fraction gradients and transition to local single-phase regions, which is a particular difficult case to handle. These two examples are also included in a list of benchmark problems specified by a group of experts at the "Workshop on Two-Phase Flow Fundamentals", see [33].

In higher dimensions finite volume methods are a natural choice to consider. However, the use of finite volume methods may not be so straightforward for the model (1), partly due to the presence of non-conservative terms. In addition, the wave structure is complicated because of interphase interactions, and upwinding may be both difficult and computationally expensive [11].

Cortes [11] considered a finite volume based numerical method for the gas-liquid two-fluid model in two dimensions. This is an upwind-type scheme based on a generalization of the density perturbation method [10]. One-dimensional computations were performed to test basic properties of the proposed scheme and a two-dimensional case was also considered which involved complex geometry and strong disequilibria. Main focus was on fast transients where the time scale was of the order of 10^{-3} sec.

Chang and Liou [6] investigated an AUSM+ type scheme in a finite volume setting for a two-fluid model similar to (1). The AUSM-approach to a large extent avoids the use of the eigenstructure of the first order system of conservation laws represented by the model (1). Several one-dimensional test cases, including the Ransom's water faucet and the air-water shock tube problem, were used to demonstrate the features of this method. Finally, many two-dimensional problems were studied where main focus was on fast transients, i.e., complicated wave phenomena taking place on a time scale of the order of $10^{-6} - 10^{-3}$ sec.

However, there seems to be relatively few examples in the literature of numerical flow cases in 2D similar to the 1D water faucet and separation flow case. These examples are characterized by strong kinematic nonequilibria as well as transition to single-phase regions.

Main objectives of this work. Concerning the above two-fluid model, the following statements taken from [31] (Chapter 11.6) seem to be highly relevant.

"Uncertainties in the correct formulation of the equations and the modelling of source terms may have a bigger impact on the result than the particular numerical model adopted. Consequently, rather than focusing on the numerics alone it makes sense to try to balance the numerical efforts with the expected fidelity of the modeling."

"The formulation of a satisfactory set of averaged-equations models emerges as the single highest priority in the modeling of complex multi-phase flows."

One important step then becomes to bring forth converged solutions for some flow cases which can reveal characteristic behavior possessed by the model. Such solutions should then be assessed in view of physical insight obtained from experiments. We hope to contribute to taking a small step in this direction by focusing on some mass transport problems which involve high kinematic disequilibria in 2D domains. Such solutions can then provide a starting point for a discussion of the physical effects associated with various terms appearing in the mathematical formulation of the model. In this process, comparison with experimental data becomes crucial, although this is beyond the scope of this work. To be more specific, the main objectives of this work are:

- Study the behavior of different wave structures when strong kinematic disequilibria are taken into account (Section 4). In particular, we focus on extensions to 2D of 1D benchmark cases like water faucet and gas-liquid separation. The motivation is to demonstrate characteristic behavior for a basic version of the two-fluid model in order to help identifying possible obvious limitations associated with the continuous model formulation.
- For the numerical computations, we employ an extension to 2D of the WIMF scheme previously studied in 1D [14]. Thus, another objective of this paper is to demonstrate the potential of the WIMF scheme when it comes to simulations of flow cases more relevant for industrial applications.
- Thirdly, we seek to illustrate (in Section 3) how the WIMF approach can be considered as an attempt to unify the two different classes of numerical methods, referred to as *segregated* and *coupled* methods. By doing so, we hope to encourage further investigations where ideas and techniques from both classes are combined to obtain schemes that can be used for simulation of more complex multi-phase purposes.

One particular motivation for developing a 2D code for the compressible gas-liquid two-fluid model, could be to pave the way for validating the use of 1D models where two-dimensional effects are

incorporated more indirectly, e.g. in the source terms that are used. For an interesting work in this direction in the context of gas flow in pipes we refer to [21].

Simplified two-phase models. We also find it appropriate to mention that there is a research activity on various simplified two-phase models. An example of such a simplified model is given in the recent works [22, 23], see also references therein, where focus is on a 1D incompressible gas-liquid model relevant for stratified and stratified wavy flow regime. The model consists of two PDEs and two algebraic relations. Different numerical discretizations of the model are explored as well as analysis of various stability criteria. This model was also studied in the earlier works [1, 2]. Other works relevant for stratified two-fluid models are represented by [20, 8]. These works deal with the derivation of simplified models and corresponding analytical and numerical solutions. Another example of a simplified 1D compressible two-phase gas-liquid model with relevance for dispersed flow is studied in [19, 18]. The purpose of these works is to study some fundamental issues related to existence of weak solutions.

The rest of this paper is organized as follows: In Section 2 we describe the transient two-fluid gas-liquid model we are interested in. Section 3 describes the discretization strategy we apply. Section 4 is devoted to numerical results for a number of test cases in 2D. We focus on natural 2D extensions of commonly used 1D test-cases. We end the paper with a few concluding remarks in Section 5.

2. A TRANSIENT TWO-FLUID MODEL

In this section we shall give more details relevant for the model (1). First, we write the model in component form using Cartesian coordinates.

$$\begin{aligned} & \partial_t \begin{pmatrix} \rho_g \alpha_g \\ \rho_l \alpha_l \\ \rho_g \alpha_g v_g^x \\ \rho_g \alpha_g v_g^y \\ \rho_l \alpha_l v_l^x \\ \rho_l \alpha_l v_l^y \end{pmatrix} + \partial_x \begin{pmatrix} \rho_g \alpha_g v_g^x \\ \rho_l \alpha_l v_l^x \\ \rho_g \alpha_g (v_g^x)^2 \\ \rho_g \alpha_g v_g^x v_g^y \\ \rho_l \alpha_l (v_l^x)^2 \\ \rho_l \alpha_l v_l^x v_l^y \end{pmatrix} + \partial_y \begin{pmatrix} \rho_g \alpha_g v_g^y \\ \rho_l \alpha_l v_l^y \\ \rho_g \alpha_g v_g^x v_g^y \\ \rho_g \alpha_g (v_g^y)^2 \\ \rho_l \alpha_l v_l^x v_l^y \\ \rho_l \alpha_l (v_l^y)^2 \end{pmatrix} \\ & + \begin{pmatrix} 0 \\ 0 \\ \alpha_g \partial_x p + \Delta p \partial_x \alpha_g \\ 0 \\ \alpha_l \partial_x p + \Delta p \partial_x \alpha_l \\ 0 \end{pmatrix} + \begin{pmatrix} 0 \\ 0 \\ 0 \\ \alpha_g \partial_y p + \Delta p \partial_y \alpha_g \\ 0 \\ \alpha_l \partial_y p + \Delta p \partial_y \alpha_l \end{pmatrix} = \begin{pmatrix} 0 \\ 0 \\ Q_g^x + M_g^x \\ 0 \\ Q_l^x + M_l^x \\ 0 \end{pmatrix} + \begin{pmatrix} 0 \\ 0 \\ 0 \\ Q_g^y + M_g^y \\ 0 \\ Q_l^y + M_l^y \end{pmatrix}. \end{aligned} \quad (2)$$

We introduce the state vector \mathbf{U} defined by

$$\mathbf{U} = \begin{bmatrix} \rho_g \alpha_g \\ \rho_l \alpha_l \\ \rho_g \alpha_g v_g^x \\ \rho_g \alpha_g v_g^y \\ \rho_l \alpha_l v_l^x \\ \rho_l \alpha_l v_l^y \end{bmatrix} \stackrel{\text{def}}{=} \begin{bmatrix} m_g \\ m_l \\ I_g^x \\ I_g^y \\ I_l^x \\ I_l^y \end{bmatrix}. \quad (3)$$

The above system contains more unknowns than equations and constitutive laws must be specified. This will be done in the following.

2.1. Equation of state for the pressure. We assume that both the gas and liquid are compressible and characterized by the following equation of states:

$$\rho_l = \rho_{l,0} + \frac{p - p_{l,0}}{a_l^2}, \quad \rho_g = \frac{p}{a_g^2}, \quad (4)$$

where a_l and a_g are the sonic speed, respectively, in liquid and gas, and $p_{l,0}$ and $\rho_{l,0}$ are reference pressure and density given as constants. We shall use the following choices

$$a_l = 10^3 \text{ m/s}, \quad a_g = \sqrt{10^5} \text{ m/s},$$

and

$$p_{l,0} = 10^5 \text{ Pa}, \quad \rho_{l,0} = 10^3 \text{ kg/m}^3.$$

Moreover, we have given the following basic constraint

$$\alpha_l + \alpha_g = 1. \quad (5)$$

2.2. Closure relations for the pressure fluctuations. It is well known that the system (1) is non-hyperbolic if $\Delta p = 0$. To make the system hyperbolic, an interfacial pressure correction term Δp of the following form [34, 30, 13, 6] is used

$$\Delta p = \sigma \frac{\alpha_g \rho_g \alpha_l \rho_l}{\alpha_g \rho_l + \alpha_l \rho_g} |\mathbf{v}_g - \mathbf{v}_l|^2, \quad (6)$$

where σ is a parameter to be chosen. Here $\sigma > 1$ ensures a hyperbolic model unless the fluid velocity difference $|\mathbf{v}_g - \mathbf{v}_l|$ becomes too large [4, 34]. In this paper we use

$$\sigma = 1.2. \quad (7)$$

Physically, Δp could represent the effects of hydrostatics or surface tension. However, the above choice (6) is motivated purely from mathematical considerations, i.e. eigenvalues become real.

2.3. Closure laws for source terms. We consider the following expression for \mathbf{M}_g and \mathbf{M}_l similar to those used in [30, 11]:

$$\mathbf{M}_l = -\mathbf{M}_g = C(\alpha_g, \rho_l, \rho_g)(\mathbf{v}_g - \mathbf{v}_l), \quad (8)$$

with

$$C(\alpha_g, \rho_l, \rho_g) = K \alpha_g \alpha_l \rho_g, \quad K = C_0 \phi(\alpha_g). \quad (9)$$

C_0 is a constant and for all the simulations in this paper we follow [14] and use

$$C_0 = 5 \cdot 10^4 \text{ s}^{-1},$$

whereas the function $\phi(\alpha_g)$ is chosen to be

$$\phi(\alpha_g) = e^{-k_1 \alpha_g} + e^{-k_2 (1 - \alpha_g)}, \quad k_1 = 50, \quad k_2 = 500. \quad (10)$$

The role of the term $\phi(\alpha_g)$ is to increase the stability properties of the scheme when transition to single-phase gas or liquid flow occurs. A similar procedure was used in [30]. For the source terms \mathbf{Q}_g and \mathbf{Q}_l we have

$$\mathbf{Q}_g = \alpha_g \rho_g \mathbf{g}, \quad \mathbf{Q}_l = \alpha_l \rho_l \mathbf{g}, \quad (11)$$

where $\mathbf{g} = (0, -9.81)$ (positive direction is upward).

2.4. Resolution of primitive variables. Having solved for the conservative variables \mathbf{U} , the primitive variables $(\alpha_g, p, v_g^x, v_g^y, v_l^x, v_l^y)$ must be obtained. For the pressure variable we see that by writing the volume fraction equation (5) in terms of the conserved variables $m_g = \alpha_g \rho_g$ and $m_l = \alpha_l \rho_l$ as

$$\frac{m_g}{\rho_g(p)} + \frac{m_l}{\rho_l(p)} = 1, \quad (12)$$

we obtain a relation yielding the pressure $p(m_g, m_l)$. This is generally a nonlinear equation which does not easily allow for an algebraic solution. Typically an iterative numerical algorithm must be used in order to obtain the pressure from (12). For the linear relations, the nonlinear equation is represented by a second order polynomial for which analytical solutions are found. Equipped with the pressure p we directly can get ρ_g and ρ_l . The volume fraction α_g is then obtained from $\alpha_g = m_g / \rho_g$.

In particular, inserting the density relations (4) in (12) we get a nonlinear pressure law $p(m_g, m_l)$ of the form

$$p(m_g, m_l) = C \left[-b(m_g, m_l) + \sqrt{b(m_g, m_l)^2 + c(m_g, m_l)} \right], \quad (13)$$

with $C = \frac{1}{2}a_l^2$ and $k_0 = \rho_{l,0} - p_{l,0}/a_l^2 > 0$ and $a_0 = (a_g/a_l)^2$ and

$$\begin{aligned} b(m_g, m_l) &= k_0 - m_l - \left(\frac{a_g}{a_l}\right)^2 m_g = k_0 - m_l - a_0 m_g, \\ c(m_g, m_l) &= 4k_0 \left(\frac{a_g}{a_l}\right)^2 m_g = 4k_0 a_0 m_g. \end{aligned} \quad (14)$$

In particular, we observe that $\alpha_g = 1$ implies that $m_l = 0$ and $m_g = \rho_g$ and

$$p(m_g, 0) = C[-(k_0 - a_0 \rho_g) + (k_0 + a_0 \rho_g)] = a_g^2 \rho_g.$$

Similarly, we observe that $\alpha_l = 1$ implies that $m_l = \rho_l$ and $m_g = 0$ and

$$p(0, m_l) = (\rho_l - \rho_0)a_l^2 + p_{l,0}, \quad \text{if } k_0 < \rho_l.$$

For $k_0 \geq \rho_l$ (i.e. $b \geq 0$) it follows that $p(m_l, 0) = 0$. In other words, the use of (13) and (14) is consistent with (4) when transition to single-phase regions occur.

Finally, the fluid velocities $\mathbf{v}_g = (v_g^x, v_g^y)$ and $\mathbf{v}_l = (v_l^x, v_l^y)$ are obtained directly from the relations

$$v_g^x = \frac{U_3}{U_1}, \quad v_g^y = \frac{U_4}{U_1}, \quad v_l^x = \frac{U_5}{U_2}, \quad v_l^y = \frac{U_6}{U_2}. \quad (15)$$

3. DISCRETIZATION STRATEGY

The two-fluid model (2) possesses fast sonic waves as well as slowly moving volume fraction waves. The large difference in wave speeds makes it difficult to obtain accurate resolution of the various wave phenomena. The Jacobian matrix (as well as corresponding eigenvalues and eigenvectors) of the above two-phase model is not given by analytical expressions. Thus, it might not be straightforward to apply modern upwind-type of schemes (Godunov and Roe type, for instance) that rely on such information. Simplified variants must be used. One example of such a simplified approach can be found in [10, 11].

The main building block in our approach is the use of central based fluxes, which require no information about wave propagation, based on splitting the flux into convective and pressure terms. This scheme is derived in Section 3.3. By carefully incorporating an upwind component in the convective terms we obtain a central-upwind type of scheme which combines the robustness of the central scheme with the accuracy of upwind based schemes, however, without making use of the underlying eigenvalue structure. This modification is described in Section 3.4. Previously, we have constructed both an explicit, a weakly-implicit, as well as a strongly implicit variant of this scheme [15, 14, 16] in a 1D setting. In this section we derive a 2D version of the weakly-implicit scheme.

3.1. The numerical scheme. We shall solve the model (2) in 2D domains by applying a standard dimensional splitting approach [27]. Assuming that we have the approximation U^n where $U^n(x, y) \approx U(x, y, t^n)$, we now want to construct an approximation U^{n+1} at the next time level t^{n+1} , such that $U^{n+1}(x, y) \approx u(x, y, t^{n+1})$. This can be achieved by considering the following sequence of operators.

$$U^{n+1} = (L_y^{\Delta t} L_x^{\Delta t}) U^n, \quad (16)$$

where the one-dimensional operator L_x^t and L_y^t , respectively, are associated with the following one-dimensional models:

$$L_x^t : \begin{cases} \partial_t(\alpha_g \rho_g) + \partial_x(\alpha_g \rho_g v_g^x) = 0 \\ \partial_t(\alpha_l \rho_l) + \partial_x(\alpha_l \rho_l v_l^x) = 0 \\ \partial_t(\alpha_g \rho_g v_g^x) + \partial_x(\alpha_g \rho_g (v_g^x)^2) + \alpha_g \partial_x p + \Delta p \partial_x \alpha_g = Q_g^x + M_g^x \\ \partial_t(\alpha_l \rho_l v_l^x) + \partial_x(\alpha_l \rho_l (v_l^x)^2) + \alpha_l \partial_x p + \Delta p \partial_x \alpha_l = Q_l^x + M_l^x \\ \partial_t(\alpha_g \rho_g v_g^y) + \partial_x(\alpha_g \rho_g v_g^y v_g^x) = 0 \\ \partial_t(\alpha_l \rho_l v_l^y) + \partial_x(\alpha_l \rho_l v_l^y v_l^x) = 0, \end{cases} \quad (17)$$

and

$$L_y^t : \begin{cases} \partial_t(\alpha_g \rho_g) + \partial_y(\alpha_g \rho_g v_g^y) = 0 \\ \partial_t(\alpha_l \rho_l) + \partial_y(\alpha_l \rho_l v_l^y) = 0 \\ \partial_t(\alpha_g \rho_g v_g^x) + \partial_y(\alpha_g \rho_g v_g^x v_g^y) = 0 \\ \partial_t(\alpha_l \rho_l v_l^x) + \partial_y(\alpha_l \rho_l v_l^x v_l^y) = 0 \\ \partial_t(\alpha_g \rho_g v_g^y) + \partial_y(\alpha_g \rho_g (v_g^y)^2) + \alpha_g \partial_y p + \Delta p \partial_y \alpha_g = Q_g^y + M_g^y \\ \partial_t(\alpha_l \rho_l v_l^y) + \partial_y(\alpha_l \rho_l (v_l^y)^2) + \alpha_l \partial_y p + \Delta p \partial_y \alpha_l = Q_l^y + M_l^y. \end{cases} \quad (18)$$

We now describe a WIMF type scheme for the discretization of the one-dimensional operators L_x^t and L_y^t similar to the one studied in [14] for solving the one-dimensional two-fluid model. We describe the solution algorithm associated with L_x^t , the algorithm for L_y^t follows by analogy.

Remark 1. *Note that it would be natural to replace the splitting (16) by a Strang splitting approach for increased efficiency [27]. Similarly, we may also use a higher order Runge-Kutta technique for the time discretization instead of a simple forward Euler step. For practical purposes it will also be crucial to incorporate higher order spatial accuracy in the discretization of the convective terms. However, for the purpose of this paper where the primary goal is to bring forth converged solutions in order to demonstrate characteristic 2D behavior, we have preferred to use first order discretization techniques on a relative fine grid. It is not surprising that the implementation of higher order accuracy require care, in particular, due to the possible transition to single-phase regions. These aspects will hopefully be addressed elsewhere.*

3.2. The one-dimensional solution operator L_x^t . We focus on the one-dimensional model (17) which we write in the following form

$$\begin{aligned} \partial_t m_g + \partial_x(I_g^x) &= 0, & m_k &= \alpha_k \rho_k, & I_k^x &= m_k v_k^x, & k &= g, l \\ \partial_t m_l + \partial_x(I_l^x) &= 0 \\ \partial_t I_g^x + \partial_x(J_g^{xx}) + \alpha_g \partial_x p &= -\Delta p \partial_x \alpha_g + Q_g^x + M_g^x, & J_k^{xx} &= I_k^x v_k^x, & k &= g, l \\ \partial_t I_l^x + \partial_x(J_l^{xx}) + \alpha_l \partial_x p &= -\Delta p \partial_x \alpha_l + Q_l^x + M_l^x \\ \partial_t I_g^y + \partial_x(J_g^{yx}) &= 0, & I_k^y &= m_k v_k^y, & J_k^{yx} &= I_k^y v_k^x, & k &= g, l \\ \partial_t I_l^y + \partial_x(J_l^{yx}) &= 0. \end{aligned} \quad (19)$$

In the following we shall briefly describe the discrete version of (19) following along the line of [17]. A more compact form of this model is given by

$$u_t + g(u)_x + a(u)h(u)_x = q(u) + m(u), \quad (20)$$

where $u = (m_g, m_l, I_g^x, I_l^x, I_g^y, I_l^y)^T$, $g = (I_g^x, I_l^x, J_g^{xx}, J_l^{xx}, J_g^{yx}, J_l^{yx})^T$, $a = (0, 0, \alpha_g, \alpha_l, 0, 0)$, $h = (0, 0, p, p, 0, 0)^T$, $q = (0, 0, -\Delta p \partial_x \alpha_g + Q_g^x, -\Delta p \partial_x \alpha_l + Q_l^x, 0, 0)^T$, and $m = (0, 0, M_g^x, M_l^x, 0, 0)^T$. Note that we have grouped the differential term $\Delta p \partial_x \alpha_k$ together with the source terms (non-differential terms) on the right-hand side of (20). The reason is that we shall use a straightforward discretization of this term which contains no numerical diffusion, see Section 3.6 for the details.

Observing that (12) defines a relation which yields the pressure $p = p(m_g, m_l)$ as a nonlinear function which depends on the masses m_g and m_l , we can derive the differential

$$dp = \kappa(\rho_l dm_g + \rho_g dm_l) \quad (21)$$

where

$$\kappa = \frac{1}{\frac{\partial \rho_l}{\partial p} \alpha_l \rho_g + \frac{\partial \rho_g}{\partial p} \alpha_g \rho_l}. \quad (22)$$

We now focus on a discretization of (20) where we for a moment neglect the source terms on the right hand side. Assuming that we have given an approximation $u^n(x) \approx u(x, t^n)$, we want to calculate an approximation $u^{n+1}(x) \approx u(x, t^{n+1})$. For that purpose, locally in the time period $[t^n, t^{n+1}]$, we consider a decomposition of (20) into the two subsystems

$$\begin{aligned} v_t + g(v+w)_x &= 0, & v(\cdot, 0) &= u^n(\cdot), \\ w_t + a(v+w)h(v+w)_x &= 0, & w(\cdot, 0) &= 0, \end{aligned} \quad (23)$$

where v and w now are the unknown variables. Setting

$$u = v + w, \quad (24)$$

adding the two equations in (23), we see that u formally is a solution of (20) with initial data $u(\cdot, 0) = u^n(\cdot)$. Thus, (23) represents a reformulation of the original model (20). We now remove some of the nonlinear coupling between the first and second subsystem of (23) by introducing the variable \tilde{h} given by

$$\tilde{h} = \tilde{h}(v) = h(v + w)|_{w=\text{const}},$$

and defining b as the Jacobian associated with $\tilde{h}(v)$

$$b := D_v \tilde{h} = D_u h. \quad (25)$$

Multiplying the first subsystem of (23) by $b = D_v \tilde{h}$, we obtain equations for $\tilde{h}(x, t)$, namely $\tilde{h}_t + b(x, t)g(v + w)_x = 0$. Thus, we approximate (23) by the the following *extended* model for (v, w, \tilde{h})

$$\begin{aligned} v_t + g(v + w)_x &= 0, & v(\cdot, 0) &= u^n(\cdot), \\ w_t + a(v + w)\tilde{h}_x &= 0, & w(\cdot, 0) &= 0, \\ \tilde{h}_t + b(x, t)g(v + w)_x &= 0, & \tilde{h}(\cdot, 0) &= h(u^n(\cdot)), \quad t \in (0, \Delta t], \end{aligned} \quad (26)$$

where $b(x, t)$ represents the Jacobian $D_u h$

$$b = D_u h = \begin{pmatrix} 0 & 0 & 0 & 0 & 0 & 0 \\ 0 & 0 & 0 & 0 & 0 & 0 \\ \kappa \rho_1 & \kappa \rho_g & 0 & 0 & 0 & 0 \\ \kappa \rho_1 & \kappa \rho_g & 0 & 0 & 0 & 0 \\ 0 & 0 & 0 & 0 & 0 & 0 \\ 0 & 0 & 0 & 0 & 0 & 0 \end{pmatrix}, \quad (27)$$

where κ is given by (22) and we have used (21). In particular, we observe that the set of equations associated with $\tilde{h}_t + b(x, t)g(v + w)_x = 0$ in (26) correspond to the *pressure evolution equation*

$$\frac{\partial p}{\partial t} + \kappa \left(\rho_1 \frac{\partial}{\partial x} (\alpha_g \rho_g v_g^x) + \rho_g \frac{\partial}{\partial x} (\alpha_1 \rho_1 v_1^x) \right) = 0. \quad (28)$$

The approximation $u^{n+1}(x)$ is obtained, in view of (24), by setting $u^{n+1}(x) = v(x, \Delta t) + w(x, \Delta t)$. Next, we propose a discretization of (26).

Remark 2. *The approach we use where the original model (20) is associated with the extended model (26), bears some similarity (in spirit) to the relaxation-based method [25] where the conservation law*

$$u_t + f(u)_x = 0, \quad (29)$$

is associated with the relaxation approximation

$$u_t + v_x = 0, \quad v_t + a^2 u_x = -\frac{1}{\varepsilon} (v - f(u)), \quad (30)$$

for an appropriate chosen constant a and small constant $\varepsilon > 0$. In the following we shall describe one natural first-order discretization of the extended model (26) which combines stability and accuracy properties such that interesting and complicated two-phase flow patterns can be calculated when a sufficiently fine grid is used. We make no attempts here to optimize the discretization of (26) but note that care must be taken, in particular, due to loss of stability associated with transition to single-phase flow.

3.3. A basic discrete scheme - XFORCE.

Method of lines. We want to construct an approximation to the model (23), which in turn is a reformulation of (20), by deriving a discrete version of the extended model (26). We consider a "method of lines" approach and solve via a two-step procedure as follows.

Step 1: We solve the first and third equation of (26) at the cell-interface $x_{j+1/2}$ by the standard Lax-Friedrichs type discretization:

$$\begin{aligned} \dot{v}_{j+1/2} + \frac{1}{\Delta x} (g_{j+1} - g_j) &= 0, & v_{j+1/2}(0) &= \frac{u_j^n + u_{j+1}^n}{2}, \\ \dot{\tilde{h}}_{j+1/2} + \frac{b_{j+1/2}}{\Delta x} (g_{j+1} - g_j) &= 0, & \tilde{h}_{j+1/2}(0) &= \frac{h(u_j^n) + h(u_{j+1}^n)}{2}, \end{aligned} \quad (31)$$

for $t \in (0, \Delta t]$ where $g_j = g(v_j + w_j)$ and $b_{j+1/2}$ is an appropriate defined average.

Step 2: Equipped with $v_{j+1/2}$ and $\tilde{h}_{j+1/2}$, we find w_j through an evolution via the second equation of (26), whereas v_j is determined through a projection. That is,

$$\begin{aligned} \dot{w}_j + \frac{a_j}{\Delta x} (\tilde{h}_{j+1/2} - \tilde{h}_{j-1/2}) &= 0, & w_j(0) &= 0, \\ \dot{v}_j &= \frac{\dot{v}_{j-1/2} + \dot{v}_{j+1/2}}{2}, \end{aligned} \quad (32)$$

for $t \in (0, \Delta t]$. Finally, in light of (24), we build an approximate solution u_j^{n+1} by employing v_j and w_j as follows:

$$u_j^{n+1} = v_j(\Delta t) + w_j(\Delta t). \quad (33)$$

Fully discrete form. First, we rewrite as follows. Combining (31) and (32), we obtain a semi-discrete scheme of the form

$$\begin{aligned} \dot{v}_j + \frac{1}{\Delta x} (g_{j+1/2} - g_{j-1/2}) &= 0, & v_j(0) &= \frac{1}{4}u_{j-1}^n + \frac{1}{2}u_j^n + \frac{1}{4}u_{j+1}^n, \\ \text{with } \dot{w}_j + \frac{a_j}{\Delta x} (\tilde{h}_{j+1/2} - \tilde{h}_{j-1/2}) &= 0, & w_j(0) &= 0, \\ & & g_{j+1/2} &= \frac{g(v_j + w_j) + g(v_{j+1} + w_{j+1})}{2}, \end{aligned} \quad (34)$$

$$\begin{aligned} \dot{v}_j + \frac{a_j}{\Delta x} (\tilde{h}_{j+1/2} - \tilde{h}_{j-1/2}) &= 0, & w_j(0) &= 0, \\ \text{with } \dot{\tilde{h}}_{j+1/2} + \frac{b_{j+1/2}}{\Delta x} (g_{j+1} - g_j) &= 0, & \tilde{h}_{j+1/2}(0) &= \frac{h(u_j^n) + h(u_{j+1}^n)}{2}. \end{aligned} \quad (35)$$

Finally, we apply a backward Euler discretization in time in (34). This gives

$$\begin{aligned} \frac{v_j^1 - v_j^0}{\Delta t} + \frac{1}{\Delta x} (g_{j+1/2}^1 - g_{j-1/2}^1) &= 0, & v_j^0 &= \frac{1}{4}u_{j-1}^n + \frac{1}{2}u_j^n + \frac{1}{4}u_{j+1}^n, \\ \text{with } \frac{w_j^1 - w_j^0}{\Delta t} + \frac{a_j}{\Delta x} (\tilde{h}_{j+1/2}^1 - \tilde{h}_{j-1/2}^1) &= 0, & w_j^0 &= 0, \\ & & g_{j+1/2}^1 &= \frac{g(u_j^{n+1}) + g(u_{j+1}^{n+1})}{2}. \end{aligned} \quad (36)$$

In order to obtain a numerical flux $\tilde{h}_{j+1/2}$ for the first equation of (35), we solve the second equation in (35) forward in time a timestep Δt , again, by applying a backward Euler discretization. This gives us a fully discrete scheme of the form

$$\begin{aligned} \frac{w_j^1 - w_j^0}{\Delta t} + \frac{a_j^0}{\Delta x} (\tilde{h}_{j+1/2}^1 - \tilde{h}_{j-1/2}^1) &= 0, & w_j^0 &= 0, & a_j^0 &= a(u_j^n), \\ \text{with } \frac{\tilde{h}_{j+1/2}^1 - \tilde{h}_{j+1/2}^0}{\Delta t} + \frac{b_{j+1/2}^0}{\Delta x} (g_{j+1}^1 - g_j^1) &= 0, & \tilde{h}_{j+1/2}^0 &= \frac{h(u_j^n) + h(u_{j+1}^n)}{2}, \end{aligned} \quad (37)$$

where $u_j^{n+1} = v_j^1 + w_j^1$, in view of (33), and $g_j^1 = g(v_j^1 + w_j^1) = g(u_j^{n+1})$. Summing (36) and (37) gives the discrete scheme

$$\frac{u_j^{n+1} - u_j^n}{\Delta t} + \frac{1}{\Delta x} (G_{j+1/2}^{n+1} - G_{j-1/2}^{n+1}) + \frac{a(u_j^n)}{\Delta x} (H_{j+1/2}^{n+1} - H_{j-1/2}^{n+1}) = 0, \quad (38)$$

where $G_{j+1/2}^{n+1/2}$ and $H_{j+1/2}^{n+1}$ are given by

$$G_{j+1/2}^{n+1} = \frac{1}{2} \begin{pmatrix} I_{g,j}^{x,n+1} + I_{g,j+1}^{x,n+1} \\ I_{1,j}^{x,n+1} + I_{1,j+1}^{x,n+1} \\ J_{g,j}^{xx,n+1} + J_{g,j+1}^{xx,n+1} \\ J_{1,j}^{xx,n+1} + J_{1,j+1}^{xx,n+1} \\ J_{g,j}^{yx,n+1} + J_{g,j+1}^{yx,n+1} \\ J_{1,j}^{yx,n+1} + J_{1,j+1}^{yx,n+1} \end{pmatrix} - \frac{1}{4\lambda} \begin{pmatrix} m_{g,j+1}^n - m_{g,j}^n \\ m_{1,j+1}^n - m_{1,j}^n \\ I_{g,j+1}^{x,n} - I_{g,j}^{x,n} \\ I_{1,j+1}^{x,n} - I_{1,j}^{x,n} \\ I_{g,j+1}^{y,n} - I_{g,j}^{y,n} \\ I_{1,j+1}^{y,n} - I_{1,j}^{y,n} \end{pmatrix}, \quad (39)$$

and

$$H_{j+1/2}^{n+1} = \begin{pmatrix} 0 \\ 0 \\ P_{j+1/2}^{n+1} \\ P_{j+1/2}^{n+1} \\ 0 \\ 0 \end{pmatrix}, \quad (40)$$

where

$$P_{j+1/2}^{n+1} = \frac{1}{2}(p_j^n + p_{j+1}^n) - \lambda[\kappa\rho]_{j+1/2}^n (I_{g,j+1}^{x,n+1} - I_{g,j}^{x,n+1}) - \lambda[\kappa\rho_g]_{j+1/2}^n (I_{1,j+1}^{x,n+1} - I_{1,j}^{x,n+1}), \quad (41)$$

with $\lambda = \frac{\Delta t}{\Delta x}$. We follow [14, 15, 16] and compute the cell interface value $[\kappa\rho_g]_{j+1/2}^n$ by using $P_{j+1/2}^n$ together with the arithmetic average $\alpha_{k,j+1/2}^n = 1/2(\alpha_{k,j}^n + \alpha_{k,j+1}^n)$ where κ is given by (22). Similarly, we obtain $[\kappa\rho]_{j+1/2}^k$.

Remark 3. As explained in [17] the above discretization, which was denoted as *X-FORCE* (*eX-tended FORCE*), represents a natural generalization of the *FORCE* scheme introduced by Toro [36]. In particular, for a nonlinear, scalar conservation law it is demonstrated that the *X-FORCE* scheme converges to the entropy weak solution.

Remark 4. The above splitting where the *h-flux* component is associated with the pressure p , and the corresponding discretization of the *g-flux*, provides a link between pressure-velocity coupled methods as used in commercial codes like, for example, *Olga* and *CFX* [31] and the theory for construction of conservative and non-oscillatory discrete schemes for nonlinear conservation laws [27].

Component form. To sum up, (38)–(41) represent a discrete version of (19) of the following form where $\lambda = \Delta t/\Delta x$ and $\delta_x a_j = (1/\Delta x)(a_{j+1/2} - a_{j-1/2})$:

- Mass equations:

$$\begin{aligned} m_{g,j}^{n+1} &= m_{g,j}^n - \Delta t \delta_x I_{g,j}^{x,n+1/2}, \\ m_{1,j}^{n+1} &= m_{1,j}^n - \Delta t \delta_x I_{1,j}^{x,n+1/2}, \end{aligned} \quad (42)$$

with

$$I_{k,j+1/2}^{x,n+1/2} = \frac{1}{2}(I_{k,j}^{x,n+1} + I_{k,j+1}^{x,n+1}) - \frac{1}{4\lambda}(m_{k,j+1}^n - m_{k,j}^n), \quad k=g,l. \quad (43)$$

- Momentum equations associated with I_k^x :

$$\begin{aligned} I_{g,j}^{x,n+1} + \Delta t \alpha_{g,j}^n \delta_x P_j^{n+1} + \Delta t \delta_x J_{g,j}^{xx,n+1/2} &= I_{g,j}^{x,n} \\ I_{1,j}^{x,n+1} + \Delta t \alpha_{1,j}^k \delta_x P_j^{n+1} + \Delta t \delta_x J_{1,j}^{xx,n+1/2} &= I_{1,j}^{x,n}, \end{aligned} \quad (44)$$

with

$$\begin{aligned} P_{j+1/2}^{n+1} + \lambda[\kappa\rho]_{j+1/2}^n (I_{g,j+1}^{x,n+1} - I_{g,j}^{x,n+1}) + \lambda[\kappa\rho_g]_{j+1/2}^n (I_{1,j+1}^{x,n+1} - I_{1,j}^{x,n+1}) &= \frac{1}{2}(p_j^n + p_{j+1}^n), \\ J_{k,j+1/2}^{xx,n+1/2} &= \frac{1}{2}(J_{k,j}^{xx,n+1} + J_{k,j+1}^{xx,n+1}) - \frac{1}{4\lambda}(I_{k,j+1}^{x,n} - I_{k,j}^{x,n}), \quad k=g,l. \end{aligned} \quad (45)$$

- Momentum equations associated with I_k^y :

$$\begin{aligned} I_{g,j}^{y,n+1} + \Delta t \delta_x J_{g,j}^{yx,n+1/2} &= I_{g,j}^{y,n} \\ I_{l,j}^{y,n+1} + \Delta t \delta_x J_{l,j}^{yx,n+1/2} &= I_{l,j}^{y,n}, \end{aligned} \quad (46)$$

with

$$J_{k,j+1/2}^{yx,n+1/2} = \frac{1}{2}(J_{k,j}^{yx,n+1} + J_{k,j+1}^{yx,n+1}) - \frac{1}{4\lambda}(I_{k,j+1}^{y,n} - I_{k,j}^{y,n}), \quad k=g,l. \quad (47)$$

Note that in order to obtain a linearly implicit scheme we should follow [16] and introduce a linearization of the convective term $J_{k,j}^{xx,n+1}$ appearing in the second equation of (45) and $J_{k,j}^{yx,n+1}$ in (47):

$$J_{k,j}^{xx,n+1} \approx I_{k,j}^{x,n+1} v_{k,j}^{x,n} := J_{k,j}^{xx,n+1/2}, \quad J_{k,j}^{yx,n+1} \approx I_{k,j}^{y,n+1} v_{k,j}^{x,n} := J_{k,j}^{yx,n+1/2}. \quad (48)$$

However, as explained in the next section, we shall take advantage of the fact that we can directly replace these central-based fluxes with simple up-wind fluxes (based on fluid velocities) together with an explicit time discretization similar to what was done in [14]. This will greatly improve the accuracy of the representation of mass fronts.

3.4. Improved accuracy for mass transport dynamic. The central type flux (modified Lax-Friedrichs) used for the convective fluxes introduces a large amount of numerical diffusion in the approximation of sharp fronts related to the masses m_g and m_l . To fix this deficiency, without destroying the stability properties of the basic scheme, we shall as gently as possible incorporate upwind flux-components in the above basic scheme (42)–(47).

The two flux components $g(u)$ and $h(u)$ in (20) are coupled through the pressure term $p(m_g, m_l)$ occurring in $h(u)$. Consequently, we may expect that the discretization of the convective terms in (42), which describes the conservation of the mass quantities (m_g, m_l) , must be carefully related to the discretization of the pressure term $p(m_g, m_l)$. This is indeed ensured by the discretization (42)–(47). In other words, we cannot simply replace the diffusive central type flux (43) used in (42) with a more accurate upwind type flux without destroying the overall stability property of the scheme. A more gentle approach must be taken where an upwind flux component is *mixed* with the central flux component (43). The implementation of this idea is described in detail in Section 3.4.2.

On the other hand, the convective terms of the momentum equations (44)–(47) are more independent. This motivates for replacing the central based fluxes (45) and (47) for the convective terms J_k^{xx} and J_k^{yx} ($k=g,l$) appearing, respectively, in (44) and (46) by simple upwind (relative to the fluid velocities) fluxes. Details are given in Section 3.4.1.

3.4.1. Convective terms of the momentum equations.

- Momentum equations associated with I_k^x :

The central *semi-implicit* flux $J_{k,j+1/2}^{xx,n+1/2}$ appearing in (44) is replaced by the *explicit* upwind flux $U_{k,j+1/2}^{xx,n}$ given by

$$U_{k,j+1/2}^{xx,n} = \frac{v_{k,j+1/2}^{x,n}}{2}(I_{k,j}^{x,n} + I_{k,j+1}^{x,n}) - \frac{|v_{k,j+1/2}^{x,n}|}{2}(I_{k,j+1}^{x,n} - I_{k,j}^{x,n}), \quad k=g,l, \quad (49)$$

where $v_{k,j+1/2}^{x,n}$ is given by the average

$$v_{k,j+1/2}^{x,n} = 1/2(v_{k,j}^{x,n} + v_{k,j+1}^{x,n}). \quad (50)$$

- Momentum equations associated with I_k^y :

The central *semi-implicit* flux $J_{k,j+1/2}^{yx,n+1/2}$ appearing in (46) is replaced by the *explicit* upwind flux $U_{k,j+1/2}^{yx,n}$ given by

$$U_{k,j+1/2}^{yx,n} = \frac{v_{k,j+1/2}^{x,n}}{2}(I_{k,j}^{y,n} + I_{k,j+1}^{y,n}) - \frac{|v_{k,j+1/2}^{x,n}|}{2}(I_{k,j+1}^{y,n} - I_{k,j}^{y,n}), \quad k=g,l, \quad (51)$$

where $v_{k,j+1/2}^{x,n}$ is given by (50).

3.4.2. Convective terms of the mass equations.

- Mass equations:

$$\begin{aligned} m_{g,j}^{n+1} &= m_{g,j}^n - \Delta t \delta_x F_{g,j}^{x,n+1/2}, \\ m_{l,j}^{n+1} &= m_{l,j}^n - \Delta t \delta_x F_{l,j}^{x,n+1/2}, \end{aligned} \quad (52)$$

where $F_{k,j}^{x,n+1/2}$ is a hybridization of the central based flux $I_{k,j+1/2}^{x,n+1/2}$ given by (43) and the upwind based flux $U_{k,j+1/2}^{x,n}$ described by (56). More precisely,

$$F_{l,j+1/2}^{x,n+1/2} = a_{j+1/2}^n I_{l,j+1/2}^{x,n+1/2} + b_{j+1/2}^n U_{l,j+1/2}^{x,n} + c_{l,j+1/2}^n \left(I_{g,j+1/2}^{x,n+1/2} - U_{g,j+1/2}^{x,n} \right), \quad (53)$$

$$F_{g,j+1/2}^{x,n+1/2} = b_{j+1/2}^n I_{g,j+1/2}^{x,n+1/2} + a_{j+1/2}^n U_{g,j+1/2}^{x,n} + c_{g,j+1/2}^n \left(I_{l,j+1/2}^{x,n+1/2} - U_{l,j+1/2}^{x,n} \right), \quad (54)$$

with

$$I_{k,j+1/2}^{x,n+1/2} = \frac{1}{2} (I_{k,j}^{x,n+1} + I_{k,j+1}^{x,n+1}) - \frac{1}{4\lambda} (m_{k,j+1}^n - m_{k,j}^n), \quad k=g,l, \quad (55)$$

and

$$U_{k,j+1/2}^{x,n} = v_{k,j+1/2}^{x,n} \frac{(m_{k,j}^n + m_{k,j+1}^n)}{2} - |v_{k,j+1/2}^{x,n}| \frac{(m_{k,j+1}^n - m_{k,j}^n)}{2}, \quad k=g,l, \quad (56)$$

where $v_{k,j+1/2}^{x,n}$ is given by (50). The coefficients appearing in (53) and (54) are given by

$$\begin{aligned} a_{j+1/2}^n &= [\kappa \rho_g \alpha_l \frac{\partial \rho_l}{\partial p}]_{j+1/2}^n, & b_{j+1/2}^n &= [\kappa \rho_l \alpha_g \frac{\partial \rho_g}{\partial p}]_{j+1/2}^n, \\ c_{k,j+1/2}^n &= [\kappa \rho_k \alpha_k \frac{\partial \rho_k}{\partial p}]_{j+1/2}^n, & k &= g, l. \end{aligned} \quad (57)$$

Remark 5. The hybridization described by (53) and (54) is motivated as follows (see also [14]): First, we observe that we have the differential relations

$$dp = \kappa (\rho_l dm_g + \rho_g dm_l), \quad d\alpha_l = \kappa \left(-\frac{\partial \rho_l}{\partial p} \alpha_l dm_g + \frac{\partial \rho_g}{\partial p} \alpha_g dm_l \right), \quad (58)$$

where κ is given by (22). We can solve for dm_g and dm_l , and we then get

$$dm_g = \alpha_g \frac{\partial \rho_g}{\partial p} dp - \rho_g d\alpha_l, \quad dm_l = \alpha_l \frac{\partial \rho_l}{\partial p} dp + \rho_l d\alpha_l. \quad (59)$$

Relation (59) motivates for introducing a flux component F_p associated with dp and F_α associated with $d\alpha_l$ such that the mass fluxes F_l and F_g in (52) are given by

$$F_l = \alpha_l \frac{\partial \rho_l}{\partial p} F_p + \rho_l F_\alpha, \quad F_g = \alpha_g \frac{\partial \rho_g}{\partial p} F_p - \rho_g F_\alpha. \quad (60)$$

F_p is associated with pressure changes dp and it is natural to define, in view of the differential relation (58)

$$F_p = \kappa (\rho_l I_g + \rho_g I_l), \quad (61)$$

where I_k is the central flux component given by (43). Similarly, F_α is associated with volume fraction changes $d\alpha_l$, and in view of (58) we define

$$F_\alpha = \kappa \left(-\frac{\partial \rho_l}{\partial p} \alpha_l U_g + \frac{\partial \rho_g}{\partial p} \alpha_g U_l \right), \quad (62)$$

where U_k is the upwind flux component (56). Inserting (61) and (62) in (60), results in the fluxes (53) and (54) with coefficients (57).

Remark 6. An important feature of the hybridization (53) and (54) is that the resulting scheme possesses the property that a pressure equilibrium is maintained under a constant velocity field for a CFL condition determined by the fluid velocity, see [14] for a detailed discussion. This feature is also explored in the first numerical example of Section 4.

Remark 7. *The above scheme is semi-implicit in the sense that we solve implicitly for the momentum $I_g^{x,n+1}$ and $I_1^{x,n+1}$, while we solve explicitly for the masses m_g^{n+1} and m_1^{n+1} as well as the y -directed momentum $I_g^{y,n+1}$ and $I_1^{y,n+1}$ along the following three steps:*

- *Firstly, we solve simultaneously for $I_{g,j}^{x,n+1}$, $I_{1,j}^{x,n+1}$, and $P_{j+1/2}^{n+1}$ from the two momentum equations given by (44) with updated fluxes (49), and the pressure equation (45). This corresponds to solving a linear problem $Ax = b$ where the matrix A possesses a band structure.*
- *Secondly, we solve for $m_{g,j}^{n+1}$ and $m_{1,j}^{n+1}$ from (52) by employing the updated momentum $I_{g,j}^{x,n+1}$ and $I_{1,j}^{x,n+1}$, obtained from the first step, in the flux (55).*
- *Thirdly, we solve for $I_g^{y,n+1}$ and $I_1^{y,n+1}$ by using (46) and (51).*

3.5. A modification to handle transition to single-phase flow. The upwind fluxes $U_{k,j+1/2}^{x,n}$, $U_{k,j+1/2}^{xx,n}$, and $U_{k,j+1/2}^{yx,n}$ involved, respectively, in (52), (44), and (46) are all of the form

$$u = \rho v,$$

for appropriate choices of ρ and v . It turns out that these upwind type fluxes are important for the accuracy of large gradients in masses. However, they often introduce instability for flow cases where the gas volume fraction α_g becomes close to 0 or 1.

In order to make the numerical scheme able to handle such flow cases we follow along the line of [14] and introduce the following modification

$$U_{j+1/2} = (1 - s_j)U_{j+1/2}^{\text{upw}} + s_j U_{j+1/2}^{\text{force}},$$

where

$$U_{j+1/2}^{\text{upw}} = v_{j+1/2} \frac{(\rho_j + \rho_{j+1})}{2} - |v_{j+1/2}| \frac{(\rho_{j+1} - \rho_j)}{2},$$

$$U_{j+1/2}^{\text{force}} = \frac{1}{2} (U_{j+1/2}^{\text{LxF}} + U_{j+1/2}^{\text{LW}}),$$

where $U_{j+1/2}^{\text{LxF}}$ and $U_{j+1/2}^{\text{LW}}$ refer to the classical Lax-Friedrichs flux and Lax-Wendroff flux, respectively. The FORCE flux $U_{j+1/2}^{\text{force}}$ [7, 36] has a stabilizing effect at transition to single-phase, however, at the price of introducing a smearing out effect. Therefore, the parameter s is chosen such that only close to single-phase flow, s becomes close to 1. Otherwise it takes values close to 0. This is implemented by setting

$$s_j = \max(\phi_j, \phi_{j+1}), \quad \phi = \phi(\alpha_g),$$

where $\phi(\alpha_g)$ is the transition fix function given by (10).

3.6. Discretization of source terms. What remains now is a description of the discretization of the term $q(u) = (0, 0, -\Delta p \partial_x \alpha_g + Q_g^x, -\Delta p \partial_x \alpha_1 + Q_1^x, 0, 0)^T$ and $m(u) = (0, 0, M_g^x, M_1^x, 0, 0)^T$ occurring on the left hand side in the momentum equations (44), see also (19). The following semi-implicit discretization is used for M_g^x and M_1^x similar to what was done in [14]:

$$(M_g^x)_j^{n+1/2} = -C(\alpha_g, \rho_1, \rho_g)_j^n \left(\frac{I_{g,j}^{x,n+1}}{m_{g,j}^n} - \frac{I_{1,j}^{x,n+1}}{m_{1,j}^n} \right), \quad (M_1^x)_j^{n+1/2} = -(M_g^x)_j^{n+1/2}. \quad (63)$$

Finally, the source term $q(u)$ is treated by a straightforward explicit and central based discretization as follows:

$$(\Delta p \partial_x \alpha_k)_j^n = \Delta p (u_j^n) \delta_x \alpha_{k,j}^n, \quad \alpha_{k,j+1/2}^n = \frac{\alpha_{k,j}^n + \alpha_{k,j+1}^n}{2}, \quad k = g, 1, \quad (64)$$

$$(Q_k^x)_j^n = Q_k^x(u_j^n).$$

4. NUMERICAL RESULTS

In this section we explore the behavior of the two-fluid model for some flow examples where characteristic 2D effects are involved. A main feature of the examples we focus on is that they involve mass transport that typically leads to transition to single-phase flow. It is well known that this is notoriously difficult for any discrete scheme to handle [31]. Consequently, we apply the first order scheme presented in Section 3, which is robust enough to handle the transition to single-phase flow in a satisfying manner. More research must be done in order to extend the WIMF approach to higher order accuracy in such a way that the simulations presented below can be handled properly. Grid refinement studies are performed for the various examples to ensure that the solutions that are presented to a large extent have converged to a limit function, i.e., that further grid refinement to a minor degree will change the solutions.

Furthermore, for the computations below we use a time step Δt determined from the stability condition

$$\Delta t = \text{CFL} \min\left(\frac{\Delta x}{a_l}, \frac{\Delta y}{a_l}\right), \quad (65)$$

where $a_l = 1000$ is the speed of sound in the liquid phase and CFL is the so-called CFL number [27]. This stability condition takes into account that transition to single-phase liquid flow may appear which implies that the maximal wave speed is determined by the speed of sound a_l .

We first, in Section 4.1, perform a test whose purpose is to verify that the 2D scheme gives correct behavior for a flow case where a gas-dominated box moves with a constant speed in a liquid dominated region under a constant pressure field. The scheme should be designed such that the uniformity of pressure and fluid velocities is not disturbed.

Next, in Section 4.2 and 4.3, we consider a natural extension of the 1-D Ransom's water faucet (see for example [32, 33]) to a 2D setting, which we shall refer to as the *waterfall* flow example. An initial liquid dominated jet corresponding to $\alpha_g = 0.2$ is surrounded by a mixture with a higher gas volume fraction corresponding to $\alpha_g = 0.4$. We compute solutions, from early transients until a steady state solution is produced showing that the initial uniform jet becomes thinner at the lower part.

Finally, in Section 4.4–4.6 we consider two different extensions of 1-D gas-liquid separation flow [9, 33]. For that purpose we consider a vertical intersection of a horizontal pipe. Again we present solutions from early times until a steady state solution has been formed.

- Firstly, we consider the case when a stagnant uniform mixture corresponding to $\alpha_g = 0.5$ is separated due to gravity only.
- Secondly, we study the behavior when the pipe initially is filled with a gas dominated mixture corresponding to $\alpha_g = 0.8$ which moves with a speed of 5 m/s in the horizontal direction. At the same time a liquid dominated mixture corresponding to $\alpha_l = 0.8$ is injected at the left end with a horizontal speed of 5 m/s.
- Finally, we extend the previous flow case by incorporating two layers which move with different speeds, an upper gas-dominated layer and a lower liquid-dominated layer. This creates an eddy-like behavior at the left inlet where a certain amount of gas is, so to speak, trapped by the water entering at the inlet.

4.1. Linear transport of a gas volume "box". In this first example we consider a square domain of length $L = 100$ m. We consider a "gas-box" placed in liquid moving with a constant velocity $v_1^x = v_g^x = 10$ m/s and $v_1^y = v_g^y = 5$ m/s, respectively, in x and y -direction. Pressure is initially constant $p|_{t=0} = 10^5$ Pa. In the first test the "gas-box", which initially is located at the center of the domain, corresponds to $\alpha_g = 0.9$ whereas the surrounding "liquid-region" corresponds to $\alpha_l = 0.9$. Results are shown in Fig. 1 for a grid composed of 200x200 cells. We consider the volume fraction α_g at time $T = 2.5$ s, and we present solutions computed by using a time step corresponding to, respectively, CFL=3.33 and CFL=50 as described by (65). The computations reveal that larger time steps give a better resolution of the gas-box. We also observe that the pressure and fluid velocities remain constant (figures are not included), as expected from the construction of the WIMF scheme described in Section 3. See also Remark 6.

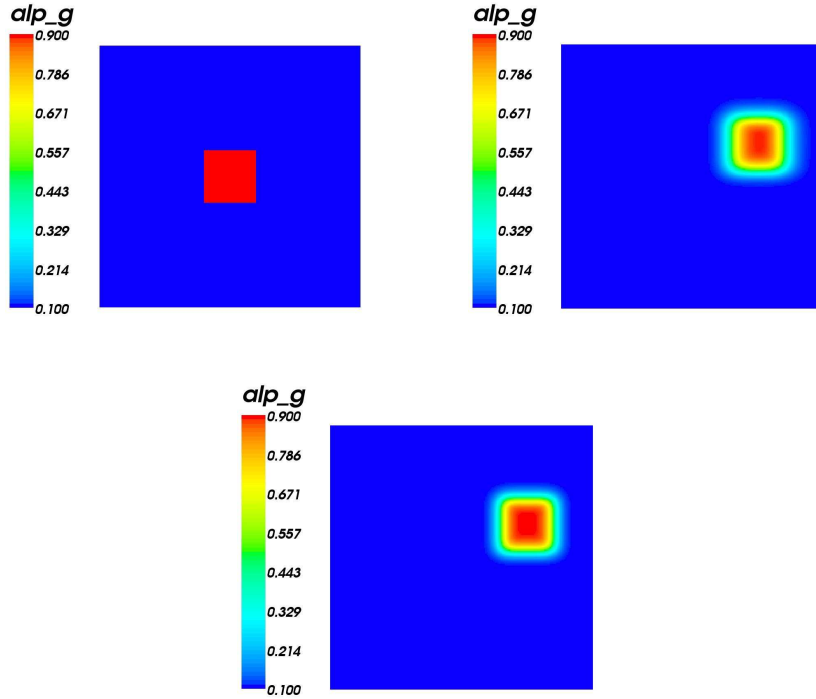


FIGURE 1. **Top:** Initial state (left) and approximate solution after $T = 2.5$ s (right) on a grid of $G = 200 \times 200$ cells with $\text{CFL}=3.33$. **Bottom:** Approximate solution with the same grid, but $\text{CFL}=50$.

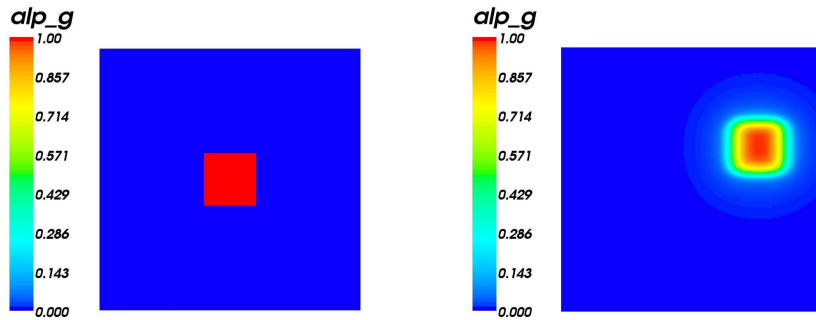


FIGURE 2. Initial state (left) and approximate solution (right) after $T = 2.5$ s on a grid of $G = 200 \times 200$ cells and with $\text{CFL}=3.33$.

In the second test, the "gas-box" corresponds to $\alpha_g = 1.0 - \varepsilon$ with $\varepsilon = 10^{-5}$ whereas the "liquid-region" corresponds to $\alpha_l = 1.0 - \varepsilon$. We compute the solution after $T = 2.5$ s on the same grid as above. It is observed that the volume fraction remains positive, and the uniformity of pressure and fluid velocities is preserved. In addition, as explained in Section 3.5, it is observed that the effect of replacing the upwind fluxes with a hybridization of an upwind and a FORCE flux, is a slightly stronger smearing-out effect. For this case we are forced to use a relatively small time step corresponding to $\text{CFL}=3.33$ in order to handle the transition to single-phase liquid flow in a stable manner.

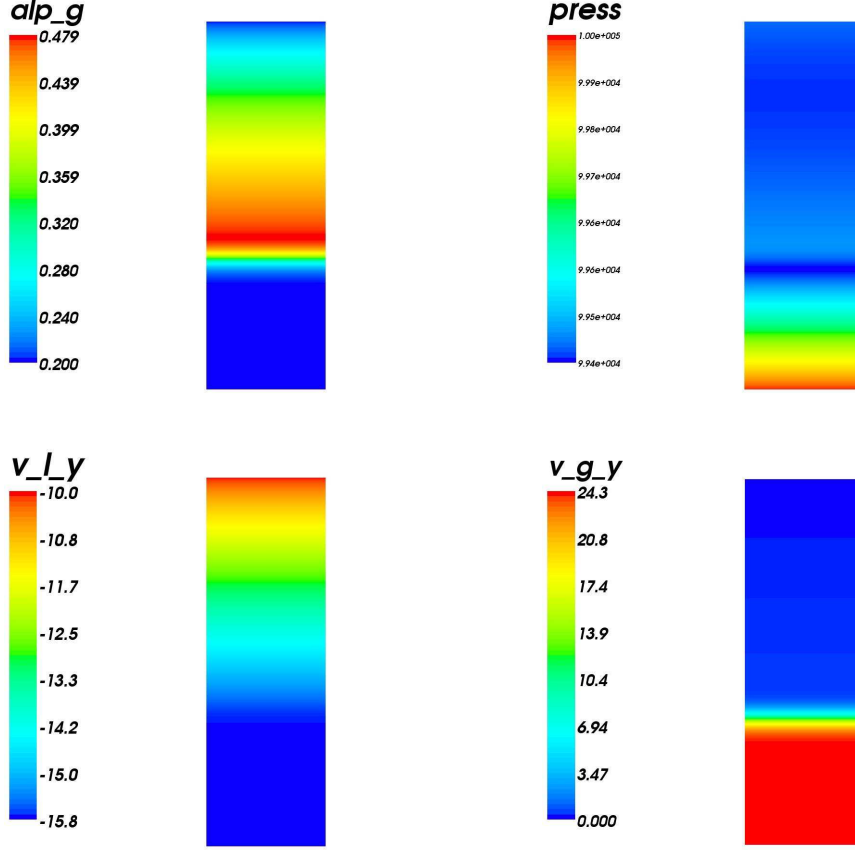


FIGURE 3. Waterfall solutions after $T = 0.6$ s with a grid of $G = 320 \times 960$ cells. **Top:** gas volume fraction α_g (left) and pressure p (right). **Bottom:** liquid velocity v_1^y (left) and gas velocity v_g^y (right)

4.2. Waterfall (1-D). We consider a quadrilateral domain of height $H = 12$ m and width $L = 3$ m. First, we want to reproduce the 1-D water faucet flow case [32, 9, 14, 30, 33, 29], but now in a 2D setting.

Initial data. Consequently, we choose as initial data

$$\alpha_g|_{t=0} = 0.2, \quad v_1^y|_{t=0} = 10 \text{ m/s}, \quad v_g^y|_{t=0} = 0 \text{ m/s}.$$

In addition, horizontal fluid velocity components are zero,

$$v_1^x|_{t=0} = 0 \text{ m/s}, \quad v_g^x|_{t=0} = 0 \text{ m/s},$$

whereas initial pressure is $p|_{t=0} = 10^5$ Pa.

Boundary data. At the top the liquid velocity is set to $v_1^y = 10$ m/s whereas gas velocity is set to $v_g^y = 0$, and $\alpha_g = 0.2$. Moreover, pressure p , as well as horizontal velocities v_1^x and v_g^x are extrapolated. Similarly, along the two vertical sides horizontal fluid velocities v_1^x and v_g^x are set to zero, whereas pressure p , volume fraction α_g , and vertical fluid velocities v_1^y and v_g^y are extrapolated. At the bottom, pressure is set to atmospheric pressure 10^5 Pa, all other variables are extrapolated.

Results. We compute solutions on a grid composed of $G=320 \times 960$ cells. Solutions are shown in Fig. 3 after $T = 0.6$ s. The result coincides directly with that obtained in [14] where comparison with an approximate analytical solution was also included. In particular, it was observed that the resolution of the gas front was similar to that of a first order Roe scheme.

4.3. Waterfall (2D). We consider the same domain as in the previous case, here denoted as R , but now decomposed into two subdomains R_1 and R_2 where $R = R_1 \cup R_2$ and

$$R_1 = \{(x, y) : 1 \leq x \leq 2, 0 \leq y \leq 12\}, \quad R_2 = \{(x, y) : 0 \leq x \leq 1 \text{ or } 2 \leq x \leq 3, 0 \leq y \leq 12\}.$$

Moreover, a water dominated jet corresponding to $\alpha_g = 0.2$ of width 1 m and associated with the region R_1 is surrounded by a fluid mixture associated with R_2 where the gas volume fraction is $\alpha_g = 0.4$. The water jet in the center of the domain moves with a vertical speed of 10 m/s (initial gas speed is zero) whereas the mixture to the left and right moves with a vertical speed of 5 m/s (initial gas speed is zero).

Initial data. Consequently, we choose as initial data

$$\alpha_g(R_1)|_{t=0} = 0.2, \quad v_1^y(R_1)|_{t=0} = 10 \text{ m/s}, \quad v_g^y(R_1)|_{t=0} = 0 \text{ m/s},$$

and

$$\alpha_g(R_2)|_{t=0} = 0.4, \quad v_1^y(R_2)|_{t=0} = 5 \text{ m/s}, \quad v_g^y(R_2)|_{t=0} = 0 \text{ m/s}.$$

In addition, the horizontal fluid velocity components are zero,

$$v_1^x(R)|_{t=0} = 0 \text{ m/s}, \quad v_g^x(R)|_{t=0} = 0 \text{ m/s},$$

whereas the initial pressure is $p(R)|_{t=0} = 10^5$ Pa.

Boundary data. At the top the liquid velocity associated with the R_1 region is set to $v_1^y = 10$ m/s whereas $v_g^y = 0$ and $\alpha_g = 0.2$. The corresponding data associated with the top of the R_2 region are $v_1^y = 5$ m/s, $v_g^y = 0$, and $\alpha_g = 0.4$. Otherwise, at the vertical sides and at the bottom, boundary data are treated as for the previous case.

Results. We compute solutions on a grid of $G=160 \times 480$ cells. Solutions are shown in Fig. 4 after a time $T = 0.6$ s. For this flow example no transition to single-phase flow appears. Consequently, the weakly implicit discretization allows us to compute solutions using large time steps corresponding to a CFL number $\text{CFL}=25$. The solutions reflect a fairly complicated flow pattern with characteristic 2D effects.

- After $T = 0.6$ s we observe from the gas volume fraction α_g that there are three characteristic gas fronts, one associated with the water jet located at the center, and another two further behind on the left and right hand side. The one at the center moves with a higher speed than the two others.
- The gas front associated with the water jet at the center, reflects a characteristic 2D pattern where the gas volume fraction is highest close to the interface between the initial R_1 and R_2 region.
- The bottom figures, which show results for the gas velocities v_g^y and v_g^x , demonstrate that there is strong upward transport effect of gas ahead of the three gas fronts (see the figure for v_g^y), which explains why the gas fronts are evolved. In addition, the horizontal velocity v_g^x indicates that gas flows toward the central water jet from both sides ahead of the gas front and the result for v_1^x shows that liquid is displaced from this region. Consequently, the part of the water jet closer to the bottom becomes thinner, see the figure for α_g .

Next we focus on the evolution of the gas volume fraction from early time $T = 0.3$ s until $T = 1.8$ s when a steady state solution has formed. Fig. 5 displays snapshots of the gas volume fraction at six different times $T = 0.3, 0.6, 0.9, 1.2, 1.5$ and 1.8 using the same grid as above. The figures reflect that only minor changes appear after $T = 1.2$ s and the steady state solution reflects the thinning effect that dominates the lower part of the water jet.

Finally, we have also included a grid refinement study in Fig. 6 for the α_g and v_1^y variable. We compare the performance for three different grids corresponding to $G_1 = 80 \times 240$, $G_2 = 160 \times 480$,

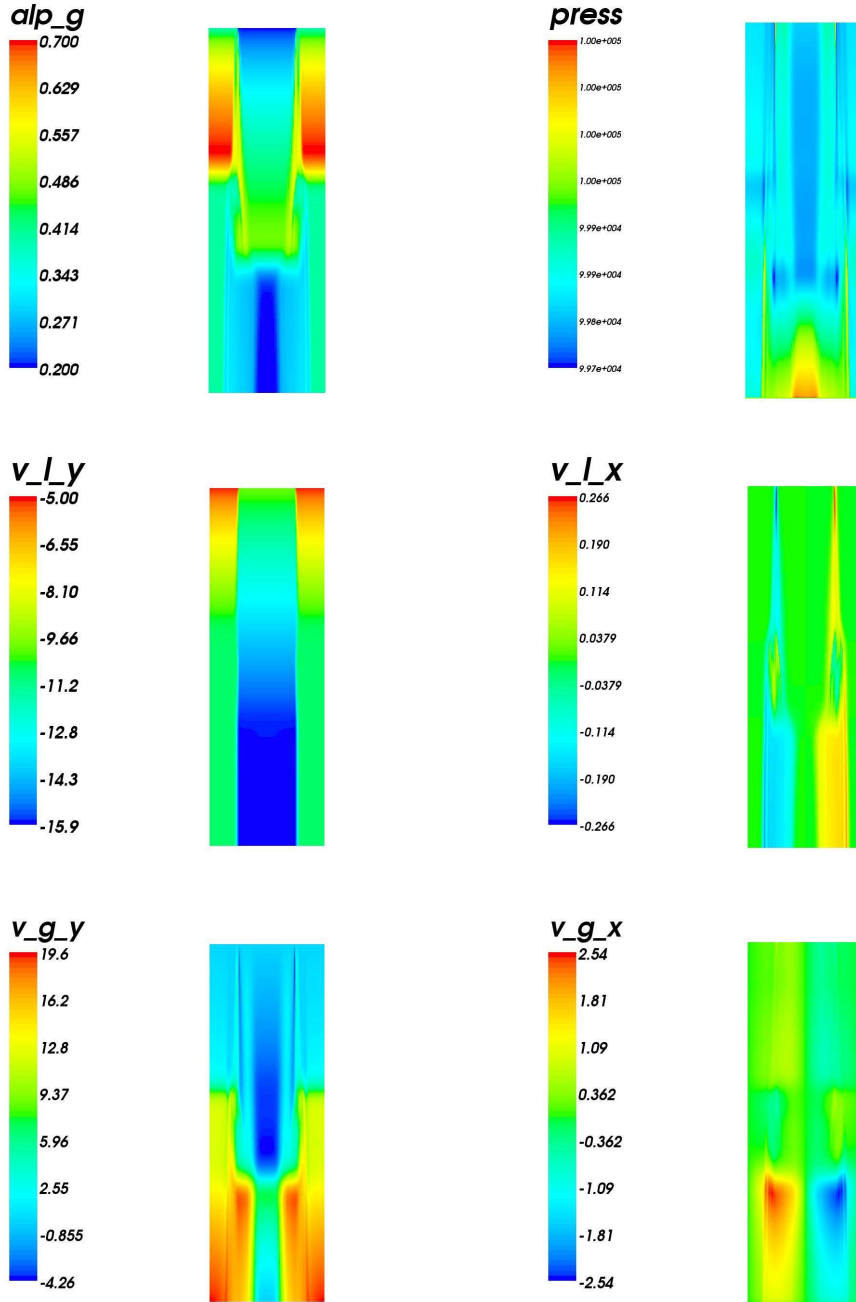


FIGURE 4. Waterfall solutions after $T = 0.6$ s on a grid of $G = 160 \times 480$ cells. **Top:** gas volume fraction α_g (left) and pressure p (right). **Middle:** vertical liquid velocity component v_1^y (left) and horizontal liquid velocity component v_1^x (right) **Bottom:** vertical gas velocity component v_g^y (left) and horizontal gas velocity component v_g^x (right).

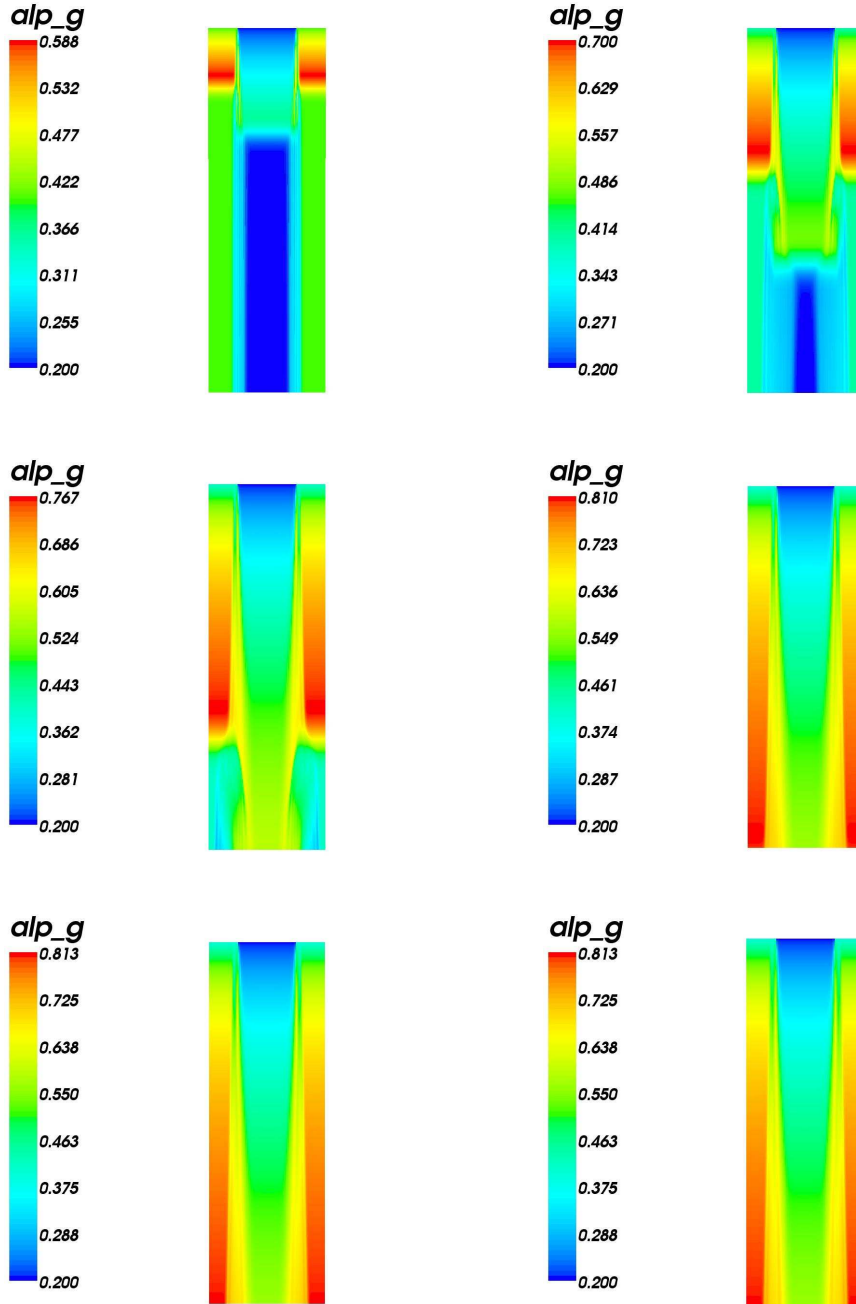


FIGURE 5. Waterfall solutions (gas volume fraction α_g) for different times with a grid of $G = 160 \times 480$ cells. **Top:** $T = 0.3$ s (left) and $T = 0.6$ s (right). **Middle:** $T = 0.9$ s (left) and $T = 1.2$ s (right) **Bottom:** $T = 1.5$ s (left) and $T = 1.8$ s (right).

and $G_3 = 320 \times 960$ cells. Minor differences between the various grids are observed, and this justifies the use of the G_2 grid for the above discussion of this flow case.

4.4. Gas Liquid Separation (1-D). We consider a domain of height $H = 0.25$ m and length $L = 3$ m. In the first case we start with a uniform mixture corresponding to $\alpha_g = 0.5$ which is at

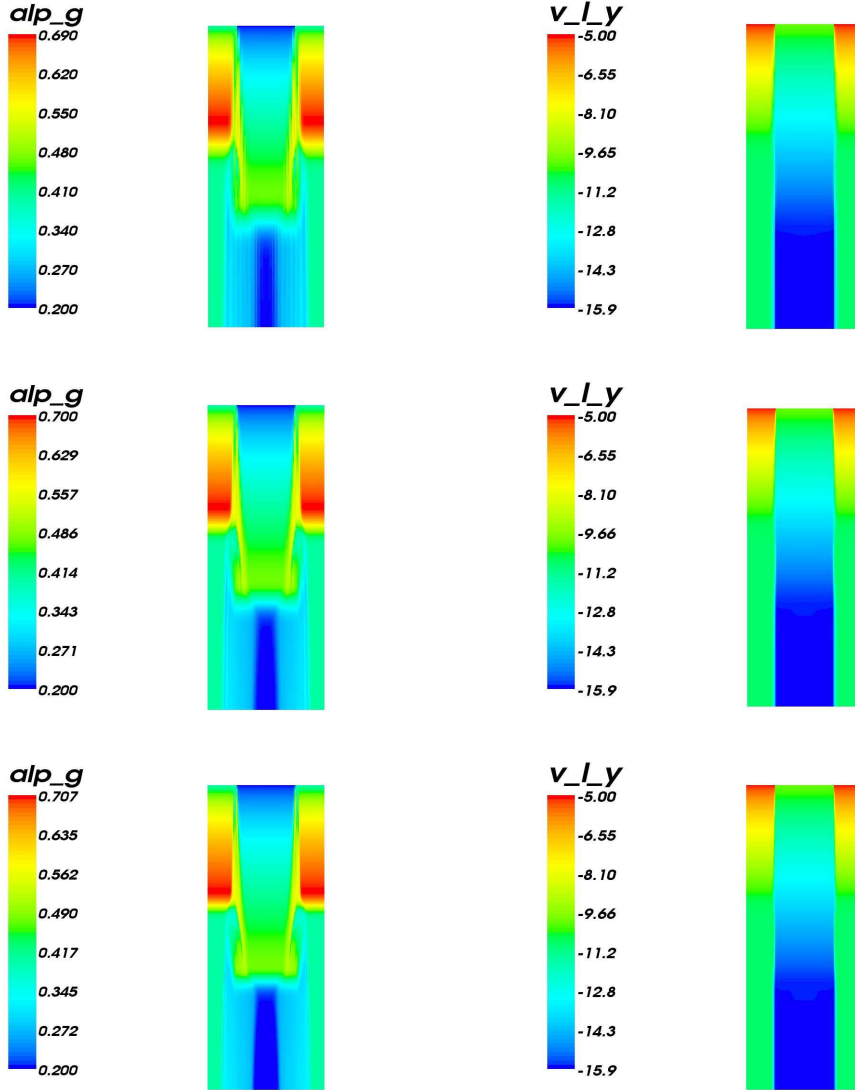


FIGURE 6. Convergence test for the waterfall example at time $T = 0.6$ s. **Left column:** Gas volume fraction α_g for different grids $G_1 = 80 \times 240$ (top), $G_2 = 160 \times 480$ (middle), $G_3 = 320 \times 960$ (bottom). **Right column:** Vertical liquid velocity v_1^y for different grids $G_1 = 80 \times 240$ (top), $G_2 = 160 \times 480$ (middle), $G_3 = 320 \times 960$ (bottom).

rest initially. Then we compute solutions as time is running and observe how gas and liquid will separate due to gravity.

Initial data. Consequently, we choose as initial data

$$\alpha_g|_{t=0} = 0.5, \quad v_1^y|_{t=0} = 0 \text{ m/s}, \quad v_g^y|_{t=0} = 0 \text{ m/s}.$$

In addition, the horizontal fluid velocity components are zero,

$$v_1^x|_{t=0} = 0 \text{ m/s}, \quad v_g^x|_{t=0} = 0 \text{ m/s},$$

whereas the initial pressure is $p|_{t=0} = 10^5$ Pa.

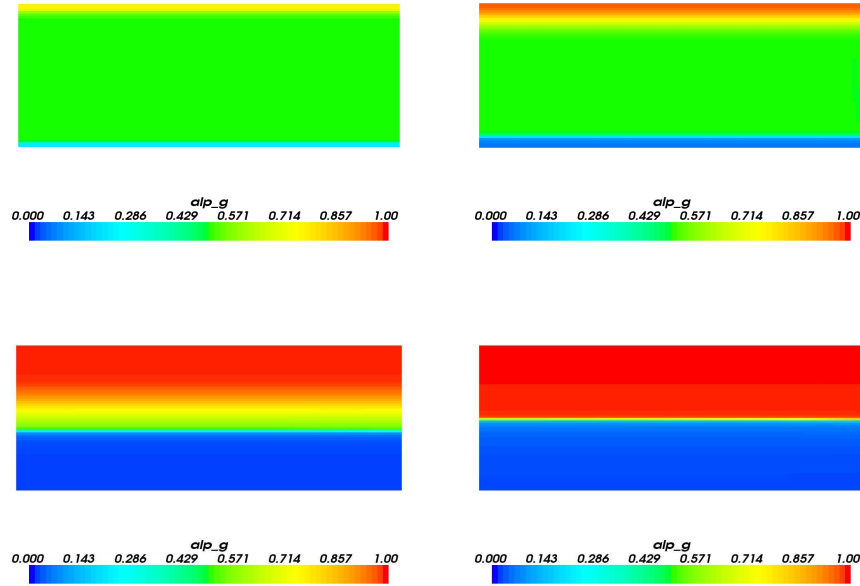


FIGURE 7. Gas-liquid separation (gas volume fraction α_g) for different times with grid $G = 100 \times 60$ cells. **Top:** $T = 0.0375$ s (left) and $T = 0.075$ s (right). **Bottom:** $T = 0.15$ s (left) and $T = 0.3$ s (right).

Boundary data. At the top and bottom, vertical velocity components v_1^y and v_g^y are set to zero (since the fluid here faces the wall), whereas horizontal velocities v_1^x and v_g^x , volume fraction α_g , and pressure p are extrapolated. The left end is closed, which implies that v_1^x and v_g^x are set to 0, while v_1^y , v_g^y , α_g and pressure p are extrapolated. The right outlet is open, in other words, the pressure is set to 10^5 Pa whereas all other variables are extrapolated.

Results. In Fig. 7 the evolution of the gas volume fraction α_g is demonstrated by displaying snapshots for different times $T = 0.0375, 0.075, 0.15$ and 0.3 s. We have used a grid of $G=100 \times 60$ cells. The WIMF scheme applied here has been verified before for this flow example by comparing with an approximate analytical solution for gas-liquid separation [14]. The figures demonstrate how two sharp mass fronts are formed, one close to the bottom which moves upward and another close to the top which moves downward. The two fronts separate the mixture region where $\alpha_g = 0.5$, respectively, from a pure liquid region (bottom) and pure gas region (top). After $T = 0.3$ s the two mass fronts have met and one large, stagnant mass front, separating the pure liquid and pure gas region, has emerged.

4.5. Separation with horizontal inflow - one layer. We consider the same domain as in the previous case. Initially the "pipe" is filled with a uniform gas-dominated mixture corresponding to $\alpha_g = 0.8$ which moves from left to right with a speed of 5 m/s. At the left inlet, a liquid-dominated mixture corresponding to $\alpha_l = 0.8$ is injected with a speed of 5 m/s.

Initial data. Consequently, we choose as initial data

$$\alpha_g|_{t=0} = 0.8, \quad v_1^y|_{t=0} = 0 \text{ m/s}, \quad v_g^y|_{t=0} = 0 \text{ m/s},$$

whereas the horizontal fluid velocity components are set as follows

$$v_1^x|_{t=0} = 5 \text{ m/s}, \quad v_g^x|_{t=0} = 5 \text{ m/s},$$

and the initial pressure is $p|_{t=0} = 10^5$ Pa.

Boundary data. At the top, bottom and right outlet boundary data are the same as for the previous case. At the inlet end, we use the data

$$\alpha_g = 0.2, \quad v_1^x = 5, \quad v_g^x = 5, \quad v_1^y = v_g^y = 0,$$

whereas the pressure p is extrapolated.

Results. In Fig. 8 we show the evolution of the gas volume fraction from time $T = 0$ until $T = 1.2$ s. A grid of $G = 100 \times 60$ cells is used. The figures reflect that the two-fluid dynamic produces a characteristic flow pattern where two different separation processes (due to gravity) take place, respectively, within the gas-dominated region on the right hand side of the pipe and the liquid-dominated region close to the left inlet. In addition, a sharp interface which separates the gas and liquid dominated region is developed. We compute the solutions from small times, where highly transient phenomena take place, up to a time where a steady state solution is produced where gas occupies the upper part of the pipe whereas the remaining lower part of the pipe is filled with liquid.

In Fig. 9 the behavior of the various quantities after $T = 0.15$ s is shown. The figures reveal a strong kinematic disequilibrium at the left inlet as liquid is driven towards the bottom by gravity and gas mainly is squeezed in the upward direction. We also observe that the horizontal fluid velocities v_1^x and v_g^x are affected by the accumulation of liquid leading to the hump-like liquid-dominated region close to the left inlet.

In Fig. 10 a grid-refinement study is presented for the α_g and v_g^y variable. We compare the performance for three different grids corresponding to $G_1 = 50 \times 30$, $G_2 = 100 \times 60$, and $G_3 = 200 \times 120$ grid cells at time $T = 0.3$. In particular, the results reflect that the use of the grid $G_2 = 100 \times 60$ to calculate the solutions discussed above should give reliable results where grid-dependent effects to a large extent is not present.

4.6. Separation with horizontal inflow - two layers. We consider the same flow domain as in the previous case, initially now filled with two layers, a gas dominated layer at the upper part corresponding to $\alpha_g = 0.8$ and a lower liquid dominated layer corresponding to $\alpha_l = 0.8$. In other words, for the domain R we set $R = R_1 \cup R_2$ where

$$R_1 = \{(x, y) : 0 \leq x \leq 3, 0 \leq y \leq 0.0125\}, \quad R_2 = \{(x, y) : 0 \leq x \leq 3, 0.125 \leq y \leq 0.25\}.$$

The upper layer moves from left to right with a speed of 5 m/s at initial time whereas the lower layer moves with a speed of 1 m/s.

At the left inlet a liquid dominated mixture corresponding to $\alpha_l = 0.8$ is injected. The injection takes place with a speed of 5 m/s at the upper part of the inlet and 1 m/s at the lower part, consistent with the initial data inside the domain.

Initial data. Consequently, we choose as initial data for R_1

$$\alpha_g(R_1)|_{t=0} = 0.2, \quad v_1^x(R_1)|_{t=0} = 1 \text{ m/s}, \quad v_g^x(R_1)|_{t=0} = 1 \text{ m/s},$$

and similarly for R_2

$$\alpha_g(R_2)|_{t=0} = 0.8, \quad v_1^x(R_2)|_{t=0} = 5 \text{ m/s}, \quad v_g^x(R_2)|_{t=0} = 5 \text{ m/s},$$

whereas the vertical fluid velocity components are set as follows

$$v_1^y(R)|_{t=0} = 0 \text{ m/s}, \quad v_g^y(R)|_{t=0} = 0 \text{ m/s}.$$

The initial pressure is $p(R)|_{t=0} = 10^5$ Pa.

Boundary data. At the top, bottom and right outlet boundary, data are the same as for the previous case. At the inlet end, for the lower layer associated with R_1 we use the data

$$\alpha_g = 0.2, \quad v_1^x = 1, \quad v_g^x = 1, \quad v_1^y = v_g^y = 0,$$

and for the upper layer associated with R_2

$$\alpha_g = 0.2, \quad v_1^x = 5, \quad v_g^x = 5, \quad v_1^y = v_g^y = 0,$$

whereas the pressure p is extrapolated.

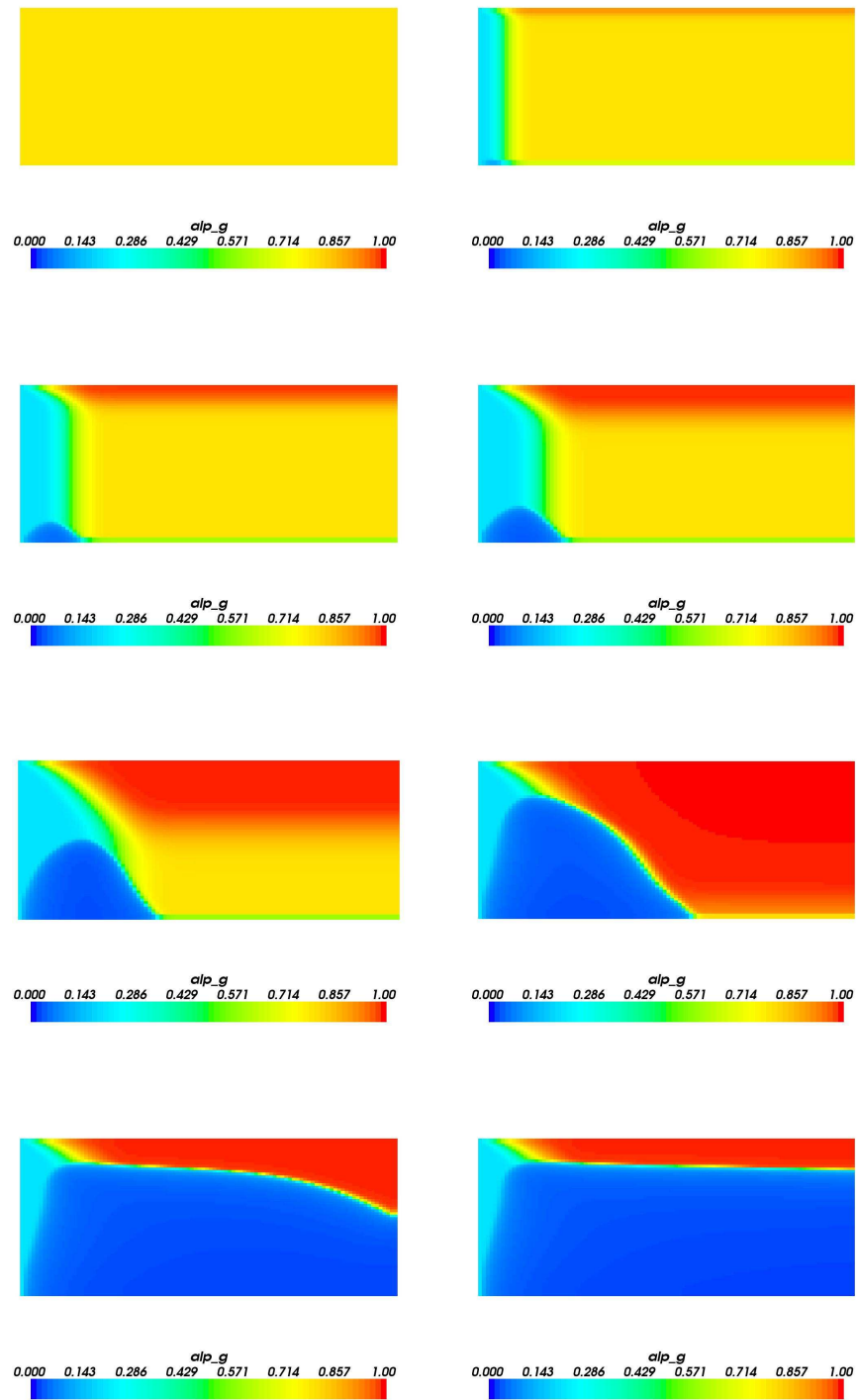


FIGURE 8. Gas-liquid separation in combination with inflow of a liquid-dominated mixture. The plots show gas volume fraction α_g for different times $T = 0, 0.0375, 0.075, 0.10, 0.15, 0.225, 0.6, 1.2$ s on a grid of $G = 100 \times 60$ cells.

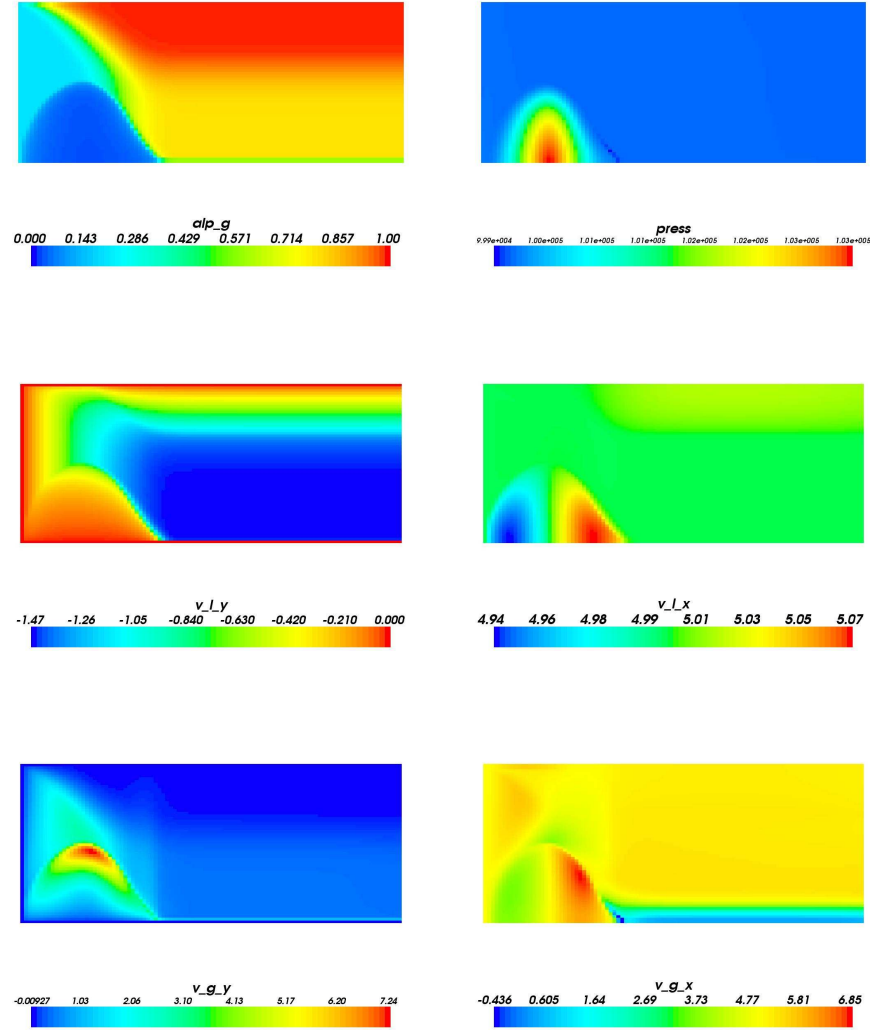


FIGURE 9. Solutions after $T = 0.15$ s with a grid of $G = 100 \times 60$ cells. **Top:** Gas volume fraction α_g (left) and pressure p (right). **Middle:** Vertical liquid velocity v_l^y component (left) and horizontal liquid velocity component v_l^x (right) **Bottom:** Vertical gas velocity component v_g^y (left) and horizontal gas velocity component v_g^x .

Results. In Fig. 11 we show the evolution of the gas volume fraction from time $T = 0$ until $T = 1.2$ s when a steady state solution has been formed. As for the previous case we employ a grid of $G = 100 \times 60$ cells. The figures reflect that the two-fluid dynamic produces a characteristic flow pattern where different separation processes (due to gravity) take place, respectively, in the upper gas-dominated region and the lower liquid-dominated region. A peculiar feature of this flow process is the eddy-like behavior of a local high-gas region which is formed close to the inlet end. Apparently, some of the gas which enters from the left inlet is not able to escape the liquid which falls towards the bottom at the left inlet. This behavior is not seen for the previous example and seems to be related to the fact that the upper layer moves with a higher speed than the lower, which implies that the inflow of water is higher at the upper layer. It is also observed that at time

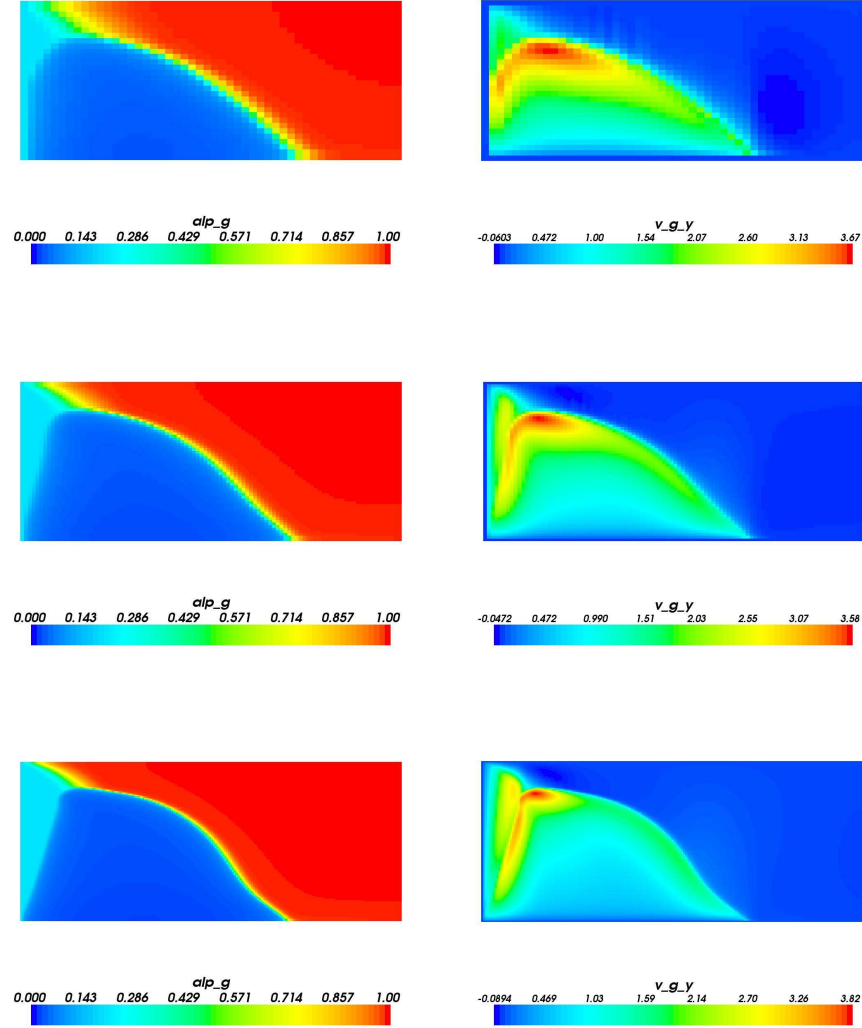


FIGURE 10. Convergence test for gas-liquid separation with inflow at time $T = 0.3$ s. **Left column:** Gas volume fraction α_g for different grids $G_1 = 50 \times 30$ (top), $G_2 = 100 \times 60$ (middle), $G_3 = 200 \times 120$ (bottom). **Right column:** Vertical gas velocity component v_g^y for different grids $G_1 = 50 \times 30$ (top), $G_2 = 100 \times 60$ (middle), $G_3 = 200 \times 120$ (bottom).

$T = 2.4$ s a steady state solution has been reached and the gas layer at the upper part occupies a considerably larger part of the pipe than for the previous example, compare with Fig. 8.

In Fig. 12 a snapshot of solutions of the various quantities at time $T = 1.2$ s is displayed. The eddy-like behavior associated with the local high-gas region close to the left inlet is more clearly explained by the figures for v_g^x and v_g^y . We observe that the gas located in the center of this high-gas region to a large extent is stagnant. At the same time there is a flow of gas mainly from all sides towards this local high-gas region. In particular, the figure of v_g^x shows that there is a transport of gas from left towards right which explains why the high-gas region will not move further into the pipe.

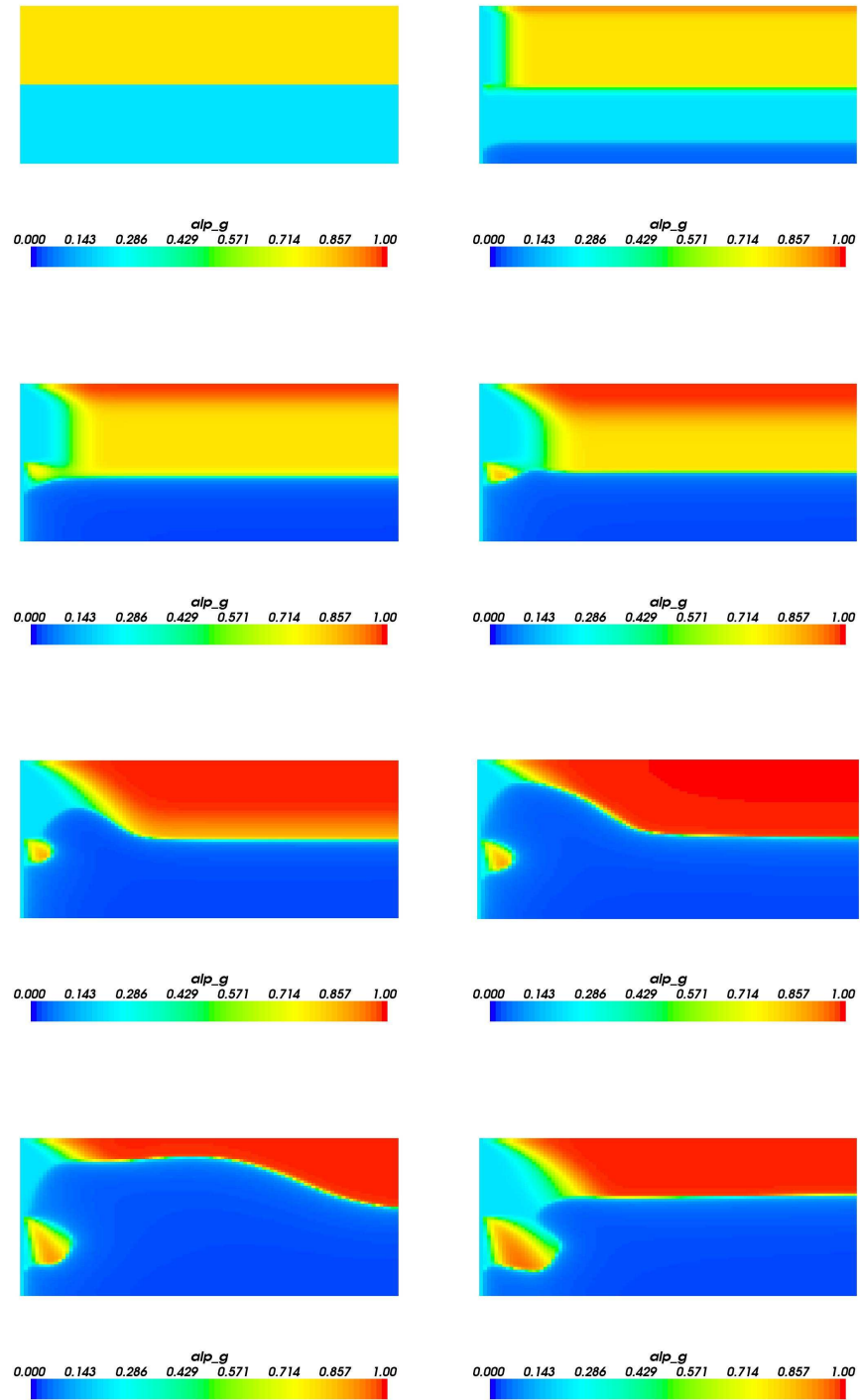


FIGURE 11. Gas-liquid separation with inflow (gas volume fraction α_g) for different times $T = 0, 0.0375, 0.075, 0.10, 0.15, 0.225, 0.6,$ and 2.4 s with a grid of $G = 100 \times 60$ cells.

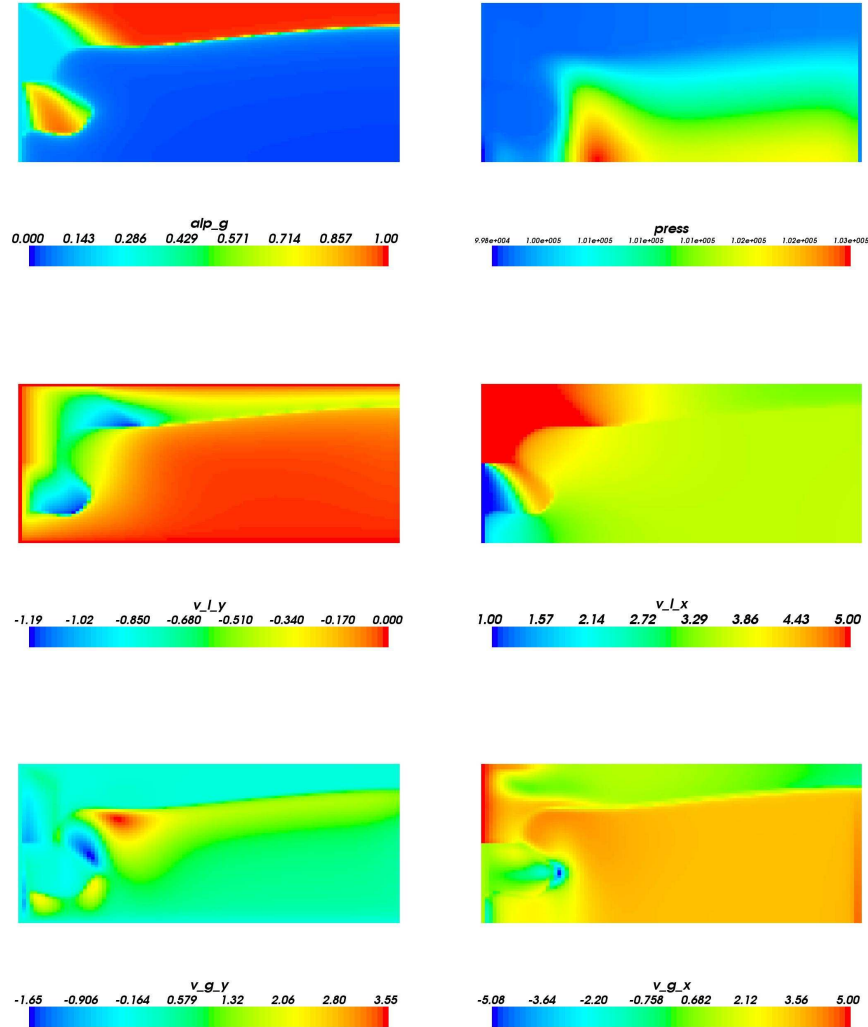


FIGURE 12. Gas-Liquid separation with inflow at time $T = 1.2$ s with a grid of $G = 100 \times 60$ cells. **Top:** Gas volume fraction α_g (left) and pressure p (right). **Middle:** Vertical liquid velocity component v_l^y (left) and horizontal liquid velocity component v_l^x (right) **Bottom:** Vertical gas velocity component v_g^y (left) and horizontal gas velocity component v_g^x (right).

In Fig. 13 a grid-refinement study is presented for the α_g and v_g^x variable. We compare the performance for three different grids corresponding to $G_1 = 50 \times 30$, $G_2 = 100 \times 60$, and $G_3 = 200 \times 120$ grid cells after $T = 0.3$ s. In particular, the results reflect that the use of the grid G_2 to calculate the solutions discussed above and shown in Fig. 11 and 12 is sufficient to capture all the main trends.

5. CONCLUDING REMARKS

We have conducted a numerical study of a common compressible gas-liquid two-fluid model in two dimensions (2D). The numerical results are carried out by using a natural extension of the WIMF method proposed in [14] in combination with a dimensional splitting approach.

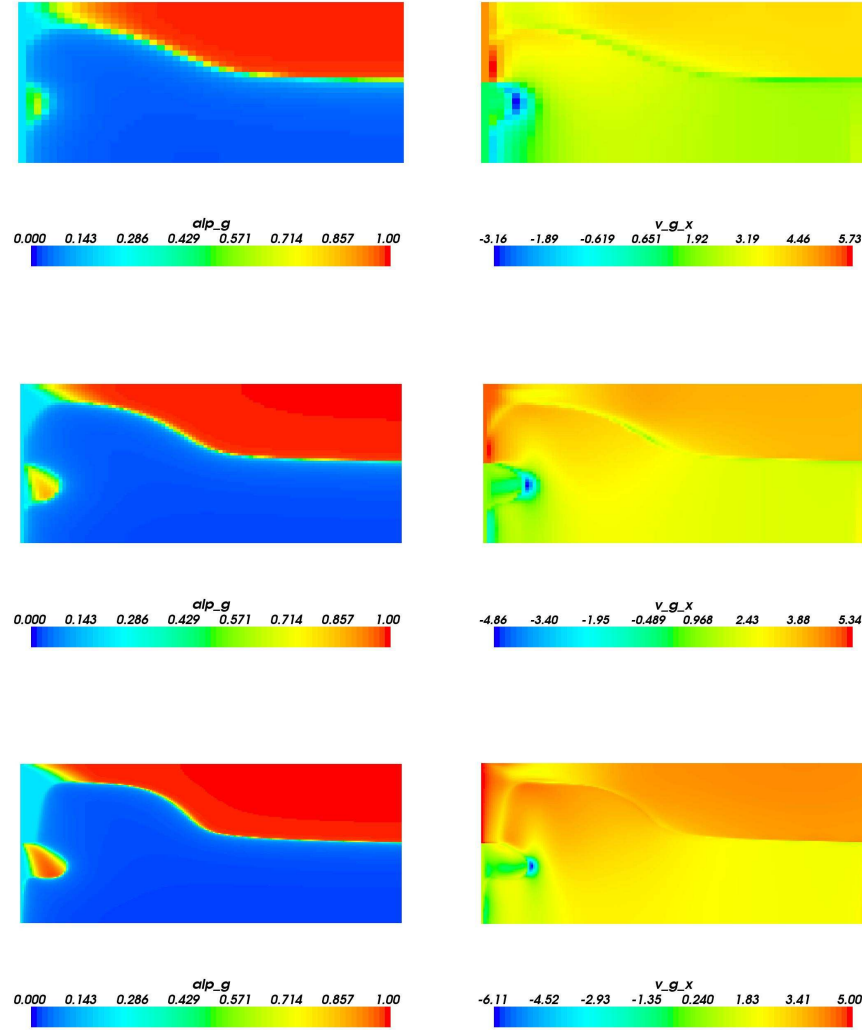


FIGURE 13. Convergence test for gas-liquid separation with inflow at time $T = 0.3$ s. **Left column:** Gas volume fraction α_g for different grids $G_1 = 50 \times 30$ (top), $G_2 = 100 \times 60$ (middle), $G_3 = 200 \times 120$ (bottom). **Right column:** Horizontal gas velocity component v_g^x for different grids $G_1 = 50 \times 30$ (top), $G_2 = 100 \times 60$ (middle), $G_3 = 200 \times 120$ (bottom).

The purpose of the two-dimensional simulations is to demonstrate characteristic two-dimensional dynamics where mass transport is essential (in contrast to pressure waves). In particular, we discuss the 2D behavior when natural extensions of common 1D benchmark tests like water faucet and gas-liquid separation are considered. These flow cases involve mass transport phenomena, highly kinematic conditions (large discrepancy between fluid velocities), and transition to local single-phase regions. In particular, we study flow cases for a 2D horizontal pipe where inflow of a two-phase mixture from one end creates various highly dynamic flow scenarios. The predicted solutions are a result of the balance between acceleration terms and gravity. The transient behavior, as well as the convergence to steady state, are computed.

These simulations motivate for further work in various directions. (i) Try to extend the scheme to include higher-order accuracy in space; (ii) Consider a finite volume discretization which allows for more general grids; (iii) Efficient calculation of steady state solutions; (iv) Extract simplified models from the full 2-D model that can be used to capture important aspects of the full model.

Acknowledgement. The first author would like to acknowledge financial support from the Research Council of Norway through the project "SAGA-GEO" under grant number 166513/V30.

REFERENCES

- [1] D. Barnea and Y. Taitel, Kelvin-Helmholtz stability criteria for stratified flow: Viscous versus non-viscous (inviscid) approaches, *Int. J. Multiphase Flow* **19**, 639–649, 1993.
- [2] D. Barnea and Y. Taitel, Nonlinear interfacial instability of separated flow, *Chem. Eng. Sci.* **49** (14), 2341–2349, 1994.
- [3] K. H. Bendiksen, D. Malnes, R. Moe, and S. Nuland, The dynamic two-fluid model OLGA: Theory and application, in *SPE Prod. Eng.* **6**, 171–180, 1991.
- [4] D. Bestion, The physical closure laws in the CATHARE code, *Nucl. Eng. Des.* **124**, 229–245, (1990).
- [5] S.J. Billett and E.F. Toro, Centred TVD schemes for hyperbolic conservation laws, *IMA J. Numerical Analysis* **20**, 47–79, 2000.
- [6] C.-H. Chang and M.-S. Liou, A robust and accurate approach to computing compressible multiphase flow: Stratified flow model and AUSM⁺-up scheme, *J. Comput. Physics* **225** (1), 840–873, 2007.
- [7] G.-Q. Chen and E.F. Toro, Centered difference schemes for nonlinear hyperbolic equations, *J. Hyperbolic Differ. Equ.* **1** (3), 531–566, 2004.
- [8] W. Choi and R. Camassa, Fully nonlinear internal waves in a two-fluid system, *J. Fluid Mech.* **396**, 1–36, 1999.
- [9] F. Coquel, K. El Amine, E. Godlewski, B. Perthame, and P. Rascle, A numerical method using upwind schemes for the resolution of two-phase flows, *J. Comput. Phys.* **136**, 272–288, 1997.
- [10] J. Cortes, A. Debussche, and I. Toumi, A density perturbation method to study the eigenstructure of two-phase flow equation systems, *J. Comput. Phys.* **147**, 463–484, 1998.
- [11] J. Cortes, On the construction of upwind schemes for non-equilibrium transient two-phase flow, *Computers & Fluids* **31**, 159–182, 2002.
- [12] D. Drew, L. Cheng, and J.R.T. Lahey, The analysis of virtual mass effects in two-phase flow, *Int. J. Multiphase Flow* **5**, 233–242, 1979.
- [13] S. Evje and T. Flåtten, Hybrid flux-splitting schemes for a common two-fluid model. *J. Comput. Phys* **192**, 175–210, 2003.
- [14] S. Evje and T. Flåtten, Weakly implicit numerical schemes for a two-fluid model, *SIAM J. Sci. Comput.* **26**, 1449–1484, 2005.
- [15] S. Evje and T. Flåtten, Hybrid central-upwind schemes for numerical resolution of two-phase flows, *ESAIM: Math. Mod. Num. Anal.* **39** (2), 253–274, 2005.
- [16] S. Evje and T. Flåtten, CFL-violating numerical schemes for a two-fluid model, *J. Sci. Computing* **29** (1), 83–114, 2006.
- [17] S. Evje, T. Flåtten, and H.A. Friis, On a relation between pressure-based schemes and central schemes for hyperbolic conservation laws, *Num. Meth. Part. Diff. Eq* **26** (2), 605–645, 2008.
- [18] S. Evje, T. Flåtten, and H.A. Friis, Global weak solutions for a viscous liquid-gas model with transition to single-phase gas flow and vacuum, *Nonlinear Analysis*, accepted, 2008.
- [19] S. Evje, K.H. Karlsen, Global existence of weak solutions for a viscous two-phase model, *J. Diff. Eq.* **245** (9), 2660–2703, 2008.
- [20] J. Grue, H.A. Friis, E. Palm, and P.O. Rusas, A method for computing unsteady fully nonlinear interfacial waves, *J. Fluid Mech.* **351**, 223–252, 1997.
- [21] M. Herty and M. Seaid, Simulation of transient gas flow at pipe-to-pipe intersections. *Int. J. Num. Meth. Fluids*, in press.
- [22] H. Holmås, D. Clamond, H.P. Langtangen, A pseudospectral Fourier method for a 1D incompressible two-fluid model. *Int. J. Num. Meth. Fluids*, in press, 2008.
- [23] H. Holmås, T. Sira, M. Nordsveen, H.P. Langtangen, and R. Schulkes, Analysis of a 1D incompressible two-fluid model including artificial diffusion. *IMA J. Appl. Math.*, in press, 2008.
- [24] M. Ishii, Thermo-fluid dynamic theory of two-phase flow, Paris: Eyrolles, 1975.
- [25] S. Jin and Z. Xin, The relaxation schemes for systems of conservation laws in arbitrary space dimensions, *Comm. Pure Appl. Math.* **55**, 235, 1995.
- [26] R.F. Kunz, D.A. Boger, D.R. Stinebring, et al., A preconditioned Navier-Stokes method for two-phase flows with application to cavitation prediction. *Comput. Fluids* **29**, 849–875, 2000.
- [27] R.J. LeVeque, Finite Volume Methods for Hyperbolic Problems, Cambridge Texts in Applied Mathematics, Berlin, 2002.
- [28] D.R. Liles and W.H. Reed, A semi-implicit method for two-phase fluid dynamics, *J. Comput. Phys.* **26**, 390–407, 1978.

- [29] S. T. Munkejord, Comparison of Roe-type methods for solving the two-fluid model with and without pressure relaxation, *Comput. Fluids* **36**, 1061–1080, (2007).
- [30] H. Paillère, C. Corre and J.R.G Cascales, On the extension of the AUSM+ scheme to compressible two-fluid models, *Comput. & Fluids* **32**, 891–916, 2003.
- [31] A. Prosperetti and G. Tryggvason (Editors), Computational Methods for Multiphase Flow, *Cambridge University Press, New York, 2007*.
- [32] V. H. Ransom, Faucet Flow, In: G. F. Hewitt, J. M. Delhay and N. Zuber, editors, *Numerical Benchmark Tests*, volume 3 of *Multiphase Science and Technology*, pages 465–467. Hemisphere/Springer, Washington, USA, (1987). ISBN 0-89116-561-4.
- [33] H. Staedtke, G. Franchello, et al., Advanced three-dimensional two-phase flow simulation tools for application to reactor safety (ASTAR), *Nuc. Eng. Design* **235**, 379–400, 2005.
- [34] J. Stuhmiller, The influence of interfacial pressure forces on the character of two-phase flow model equations, *Int. J. Multiphase Flow* **3**, 551-560, 1977.
- [35] V.A. Titarev and E.F. Toro, MUSTA schemes for multi-dimensional hyperbolic systems: analysis and improvements, *Int. J. Num. Meth. Fluids* **49** (2), 117–147, 2005.
- [36] E.F. Toro, *Riemann Solvers and Numerical Methods for Fluid Dynamics*, 2nd Ed. Springer-Verlag: Berlin, 1999.
- [37] I. Toumi and A. Kumbaro, An approximate linearized riemann solver for a two-fluid model, *J. Comput. Phys.* **124**, 286–300, 1996.